RECONFIGURABLE ANTENNAS USING VARACTORS ON A PLANAR PARASITIC LAYER AND PIN DIODES ON A DOME PARASITIC LAYER

by

Andrew J. Hendricks

A thesis submitted in partial fulfillment
of the requirements for the degree

of

MASTER OF SCIENCE

in

Electrical Engineering

Approved:

Bedri A. Cetiner, Ph.D. Major Professor	Reyhan Baktur, Ph.D. Committee Member
T. C. Shen, Ph.D. Committee Member	David F. Feldon, Ph.D. Vice Provost of Graduate Studies

UTAH STATE UNIVERSITY
Logan, Utah

2026

ABSTRACT

Reconfigurable Antennas Using Varactors on a Planar Parasitic Layer and PIN Diodes on a Dome Parasitic Layer

by

Andrew J. Hendricks, Master of Science

Utah State University, 2026

Major Professor: Bedri A. Cetiner, Ph.D.
Department: Electrical and Computer Engineering

Reconfigurable antennas allow variation in radiation patterns, polarization, and/or operating frequency. Reconfiguring radiation patterns allows increased signal-to-noise ratio by receiving signals from desired directions and rejecting signals from unwanted directions. Such selectivity is important for wireless applications of all types, but is of particular importance to radar systems, satellite communications, and advanced wireless communications.

This research investigates two variants of a C-band, 5 GHz reconfigurable antenna utilizing spherical and planar pixelated parasitic layers. The research uses Ansys High-Frequency Structure Simulator (HFSS), a full-wave electromagnetic simulation tool, to simulate antenna behavior. The antenna is based on previous research that achieved discrete beamsteering using PIN diodes on a planar parasitic layer [1, 2]. The first variant achieves continuous beam steering between $\theta \in \{-23°, 23°\}; \phi = 0°$ and $\theta \in \{-29°, 29°\}; \phi = 90°$. The antenna operates by varying coupling between copper pixels on a planar parasitic layer using varactor diodes. The second variant achieves wide-view beam steering between $\theta \in \{-52°, 50°\}; \phi = 90°$ using PIN diodes to couple copper pixels on a spherical parasitic layer.

The first variant builds on previous work with the novelty of a sub-6 GHz operation with varactor diodes to achieve continuous beamsteering. The second variant builds on previous work to demonstrate wide-angle beamsteering with improved gain over the planar parasitic layer.

(93 pages)

PUBLIC ABSTRACT

Reconfigurable Antennas Using Varactors on a Planar Parasitic Layer and PIN Diodes on a Dome Parasitic Layer

Andrew J. Hendricks

This research explores two types of reconfigurable, steerable antennas. These antennas change their beam direction based on electric input signals. The antennas have a layer that overlays the main antenna circuit board. The layer has small copper rectangles (pixels) that may be connected using either varactor diodes (which behave as voltage-controlled capacitors) or PIN diodes (electronic switches). The first antenna can steer in the xz-plane in any direction within about 23° from boresight (straight up from the antenna) and in the yz-plane to about 29° from boresight. The antenna uses varactor diodes on a planar layer. The second antenna can tilt its beam much farther, about 50° from boresight. The second antenna uses PIN diodes on a spherical layer to connect the copper pixels. The antennas were simulated in HFSS, a full-wave EM simulation software, and the latter antenna was constructed and measured.

To all the peoples of the world; may this research help you live longer, happier, freer, and become all you are meant to be.

ACKNOWLEDGMENTS

I am grateful that my advisor, Dr. Cetiner, helped me complete this research. A special thanks to Joshua Christiansen and Evan Gobien for their assistance in modeling and measuring the fabricated antennas and perfecting the HFSS simulations. Another thanks to TTM Technologies in Logan, who fabricated the antennas and gave productive feedback.

I am immensely grateful to my professors, Dr. Held, Phillips, Heavilin, Moon, Powell, Budge, Jost, Swenson, Watson, Cripps, Droge, Gunther, Ahbi, Sarsilmaz, Hancock, and Zhang, and especially to Diane and Tricia, for their support throughout the years and in the development of this thesis. I am grateful for my friends, especially Bradley Baker, Jordan Tcrka, Tyler Blevins, Kyle and Stephanie Mooty, Parker, Jarom, Chaz Cornwall, Nik Clark, Ryan Kirby, Tom and Sam Christiansen, Zack Bell, Thomas Bradshaw, Tanner Dalde, Jacob Bybee, Alan Merritt, Joseph and Amanda Stringham, Jonah, Caleb, and Micah Black, Sean Peacock, Andrew Crook, Alexis Evans, Dave Pipkin, Daniel Henshaw, David Rowbotham, Derek Redmond, Jordan Johnson, Ben Lewis, Justin Wellington, Trent Chipman, and Cole Francis, for teaching me about engineering and being good examples.

And last, I am profoundly grateful to my family for teaching me, supporting me, and giving me multitudinous opportunities to grow and learn.

Andrew J. Hendricks

CONTENTS

LIST OF TABLES

LIST OF FIGURES

ACRONYMS

ABS	Acrylonitrile Butadiene Styrene
AEM	Additive Electronic Manufacturing
CV	Capacitance/Voltage
dB	Decibel
DC	Direct Current
DUT	Device Under Test
EM	Electromagnetic
FET	Field-Effect Transistor
FPGA	Field-Programmable Gate Array
GA	Genetic Algorithm
GPS	Global Positioning System
HDT	Heat Deflection Temperature
HFSS	Ansys High Frequency Structure Simulator
in	inch
LHCP	Left-handed Circular Polarization
MEMS	Micro-Electro-Mechanical Systems
MGP	Maximum Gain Point
oz	Ounce
PCB	Printed Circuit Board
PET-G	Polyethylene Terephthalate Glycol
PIN	Positive-Intrinsic-Negative
PLA	Polylactic Acid
PML	Perfectly Matched Layer
PPL	Planar Parasitic Layer
PRS	Parasitic Reflective Surface

RA	Reconfigurable Antenna
RF	Radio Frequency
RHCP	Right-handed Circular Polarization
RL	Return Loss (-S11)
RLC	Resistance-Inductance-Capacitance
SMA	Sub-Miniature version A
SPL	Spherical Parasitic Layer
SWaP	Size, Weight, and Power
T/R	Transmit/Receive
UAV	Unmanned Aerial Vehicle
UPC	Technical University of Catalonia—Barcelona Tech, Barcelona, Spain
USU	Utah State University
UHF	Ultra High Frequency (300-3 GHz)
VNA	Vector Network Analyzer
θ_{3dB}	3-dB beamwidth measured in the yz-plane
λ	Wavelength
ϕ_{3dB}	3-dB beamwidth in xz-plane
§	Section

CHAPTER 1

INTRODUCTION

Antenna beamsteering is the change in direction of maximum gain of an antenna. Antenna beamsteering can decrease unwanted received signals (e.g. noise, clutter, interference, or jammers), allow more signals per area via spatial multiplexing [1], focus energy towards or from a target or another antenna, improve link budgets, and increase system bandwidth, among other purposes. Various beamsteering methods exist, including phased-array antennas, mechanically steered antennas, and reconfigurable antennas (RAs) [1,2,6,7]. However, requirements for size, weight, and power (SWaP), cost, high voltage requirements, turning speed [6], grating lobes at large angles, limited bandwidth, limited lifetime, and controller availability can be prohibitive for many systems.

Reconfigurable antennas (RAs) are individual antenna elements capable of changing gain, beam pattern, polarization, or bandwidth given suitable inputs [6,8]. This research investigates an RA that consists of a reconfigurable parasitic layer that overlays a patch antenna. This RA provides a stationary antenna that avoids the use of complicated electronics on the antenna itself, thus avoiding several issues with phased array and mechanically steered antennas, such as grating lobes, mechanical wear, and individual phase shifters, amplifiers, and transmit/receive (T/R) modules for each array element. Use of RAs in phased-array antennas allows for variation in element factor, which contrasts sharply with previous types (such as dipoles), where element factor is fixed.

Various RA architectures have been investigated [1, 6, 9, 10]. One RA type includes switchable or tunable nonresonant conductive pixels, which may be arranged as a reconfigurable reflector [10], a planar parasitic layer [1, 6, 9], or a spherical parasitic layer [2, 11]. Switching may be performed by PIN diodes [1, 2, 6, 9, 10], radio frequency (RF)-micro-electronic-mechanical devices (MEMS) [6, 10], field-effect transistors (FETs) [12], or optoelectronics [6]. Variable coupling or tuning may be accomplished using varactor diodes

[6,10,11,13] or varistors, which act as voltage-controlled capacitors or resistors, respectively. Switching methodologies permit many different modes, but only allow discrete ON and OFF states for each switch. Varactor diodes allow continuous capacitance variation with voltage. Varactor diodes also use comparatively little current and power. [14]

This research will focus on an aperture-fed patch antenna with a parasitic layer. The parasitic layer will have two variants - a planar form, such as in [1]. See Fig. 1.1 and a spherical form, such as in [2] as seen in Fig. 1.2. The planar form will be reconfigured by varactor diodes and operate at 5 GHz. The varactor diodes address the need for a finely-steered beam. This antenna will be novel in that it is the first varactor-based planar-parasitic-surface RA in a sub-6 GHz band. The spherical form will be reconfigured by PIN diodes and operate around 4.75 GHz. The spherical layer, being equidistant from the patch radiator, may improve the beam steering angle. This antenna will be novel in the use of PIN diodes to connect pixels mounted on a pixelated spherical parasitic layer (SPL).

In short, the research contributes the following:

1. Demonstrate the utility of varactor diodes for antenna beamsteering using reconfigurable antennas (RAs) based on a planar parasitic layer.

2. Demonstrate the utility of varactor diodes for sub-6 GHz RAs.

3. Demonstrate fine beam steering using varactor diodes on a planar parasitic layer for RAs.

4. Demonstrate a wider beam steering range (i.e. wider field of view) using PIN diodes in spherical parasitic layer RAs relative to a planar parasitic layer RA.

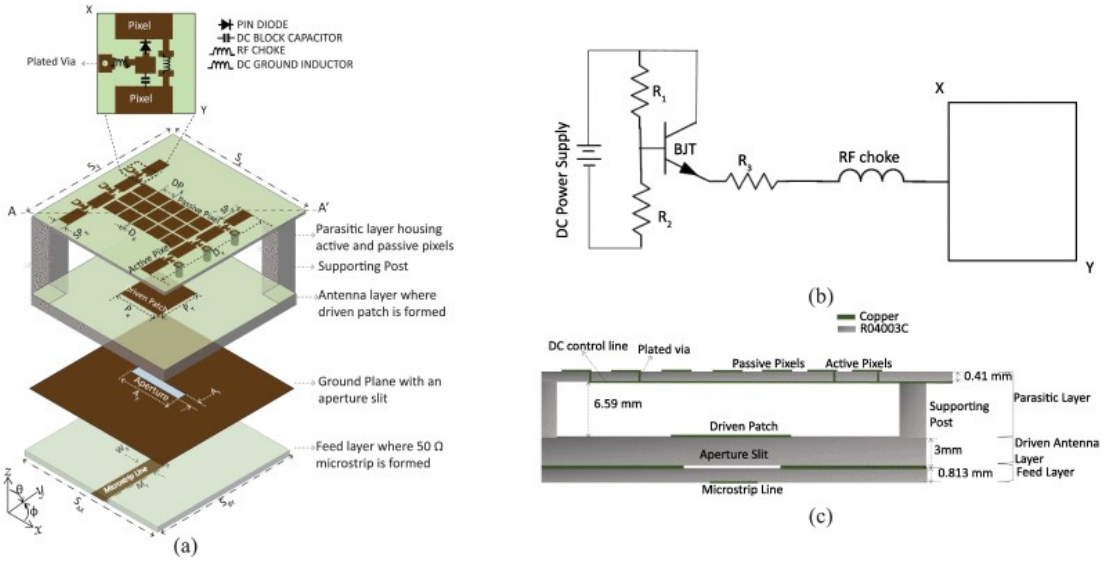

Fig. 1.1: Antenna designed in [1] ©2018 IEEE.

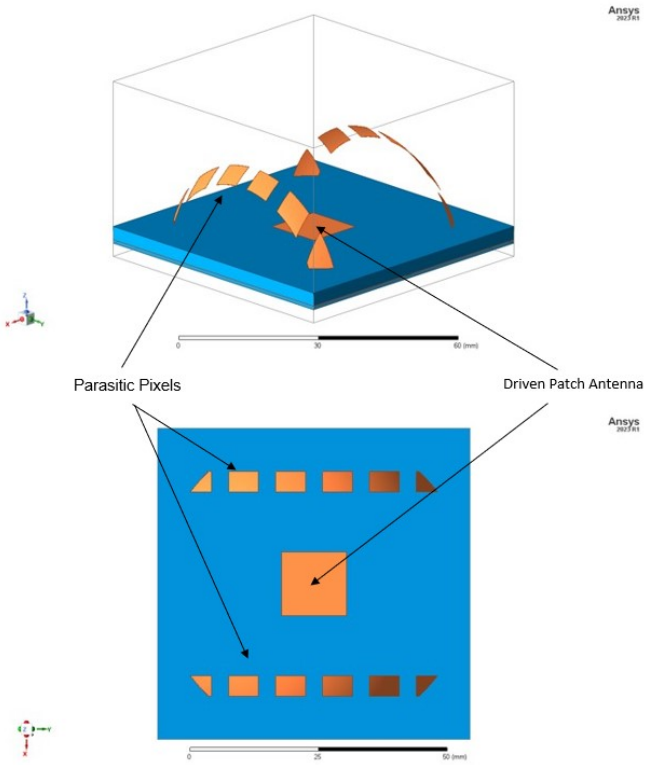

Fig. 1.2: Antenna simulated and reported in [2].

CHAPTER 2

Background

2.1 Patch Antennas

Patch antennas were introduced in 1972 by Munson [15], followed by Howell [16], and initially published in 1974 [17]. Patch antennas consist of a conductive patch (which can be any shape, although rectangular and circular are most common) mounted over a dielectric substrate over a metallic ground plane [18]. Since then, patch antennas have become very popular due to the ease of fabrication on printed circuit boards (PCB). Patch antennas are an integral part of certain types of reconfigurable antennas (RAs) [1, 8]. Basic patch antennas have large beamwidths [18], with $\theta_{3dB} \approx 30^\circ$ and $\phi_{3dB} \approx 60^\circ$, where θ_{3dB}, ϕ_{3dB} are the 3-dB beamwidths of the antenna in the xz- and yz-planes respectively. The patch antenna is considered to lie in the xy-plane. See Fig. 2.1. Equations for the radiation pattern are given in [18, 19].

Patch antennas are electrically equivalent to resonant cavities between the patch and ground plane. Fringing fields along the edges of the patch yield radiation [18]. Munson [17] states feed lines that are perpendicular to the radiating electric field and are electrically close to the ground plane do not significantly affect the radiation pattern. However, feedlines may still be a concern based on the antenna geometry [5].

Patch antennas may be fed directly via coaxial or microstrip feeds, or indirectly via apertures or proximity-coupled feeds. [18]. Direct feeds offer ease of manufacture and reduced backlobe radiation. Aperture-coupled feeds offer reduced feedline radiation and allow thick substrates. Aperture-coupled feeds also allow for more symmetric radiation patterns in the main lobe due to reduced radiation from the feedline. However, aperture-fed patch antennas have increased backlobe radiation compared to direct-fed antennas. Proximity-

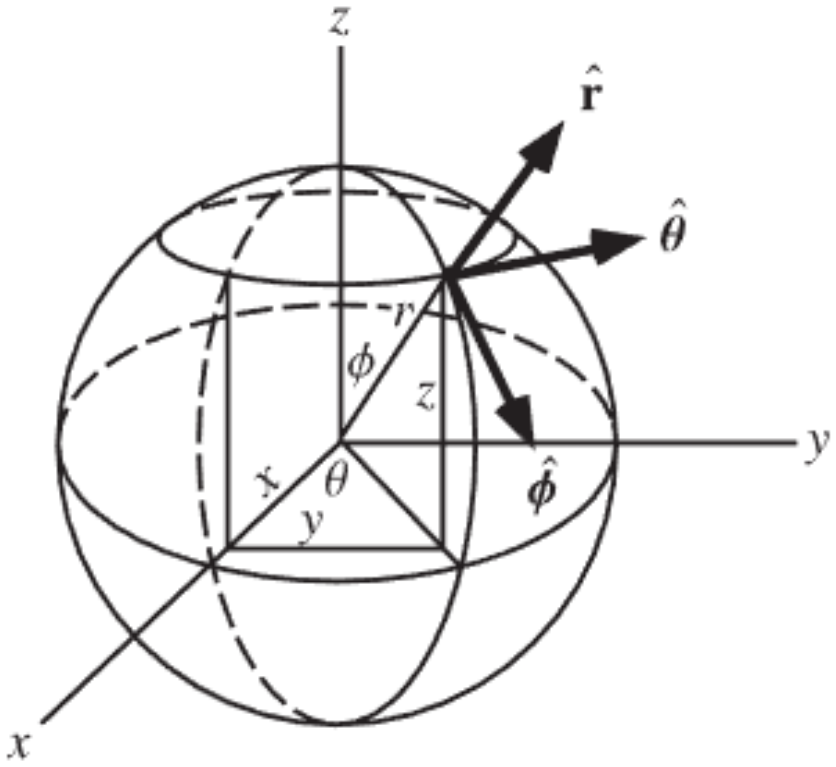

Fig. 2.1: Spherical Coordinates [3]

coupled feeds reduce feedline radiation, but requires multilayer fabrication. [18] This research utilizes an aperture-coupled feed to allow for more symmetric radiation patterns.

Bandwidth is determined by the substrate thickness and antenna geometry. [18, 20]. Larger bandwidths may be achieved by placing multiple patches above each other [20].

2.2 Reconfigurable Antennas

RAs permit changing antenna properties while in use, such as gain, polarization, operational frequency, beamwidth, and radiation pattern via changing current flow over the aperture. [1, 6]. This research uses a pixelated RA architecture described as follows in [4]: "[Fig. 2.2] shows a generic individual [RA] structure consisting of three layers, namely, feed–, antenna–, and parasitic–layer. Reconfigurable modes of operations in frequency of operation, polarization and radiation pattern are generated by controlling the electromagnetic (EM) mutual coupling that occurs between a driven antenna and parasitic layer placed in the

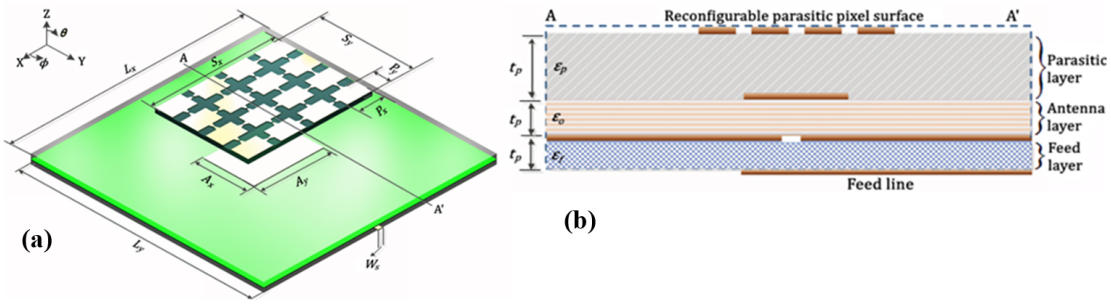

Fig. 2.2: (a) 3D schematic and (b) cross-sectional view of a generic state-of-the-art [RA] architecture with key design parameters. (S_x, S_y); lateral size of the reconfigurable parasitic pixel surface, (p_x, p_y); individual pixel dimensions, (A_x, A_y); driven antenna size, (L_x, L_y); size of the ground metallization, $(\epsilon_f, \epsilon_a, \epsilon_p)$; relative dielectric constants of the feed-, antenna- and parasitic layer-substrate, (t_f, t_a, t_p); thicknesses of the feed-, antenna- and parasitic-layer [4].

near-field of the driven antenna. On the surface of the parasitic layer there exists a number of electrically small metallic pixels optimized in terms of number and geometry, which are interconnected by RF switches. This surface is called reconfigurable parasitic pixel surface as its reactive loading, and thus EM mutual coupling between driven antenna and parasitic layer is varied by controlling the ON- and OFF- states of interconnecting switches, where each set of switch configuration corresponds to a different mode of operation in terms of frequency of operation, polarization, and radiation pattern [21]."

A spherical parasitic layer is expected to have improved coupling to the radiated field from the driven patch antenna. This arises from the near-spherical phase front in the near-field of a patch antenna [4]. As a result, the maximum beamsteering angle and gain is expected to be greater than the planar parasitic layer.

The use of reconfigurable antennas may allow wideband operation [9, 20], rapid beam-steering, changes in gain, and dynamic spatial-division multiplexing [1]. In turn, these properties "help improve the system performance, communication security, and energy efficiency by directing signals toward the intended directions while reducing interference in unintended directions." [1, 7] Arrays of RAs may be used to enhance beamforming capabilities [22].

Various RA schemes exist, including electrical, mechanical, optical, and material change techniques [6, 9, 23]. This thesis focuses on electrical RAs.

Various RA architectures have been investigated [1, 6, 9, 23]. One RA type includes switchable non-resonant conductive pixels including reconfigurable reflectors [10], planar parasitic layers [1, 6, 9], or spherical parasitic layers [2, 11]. The switching may be accomplished by PIN diodes [1, 2, 6, 9, 10, 23], RF-MEMS [6, 10, 23], FETs [12], or optoelectronic switching [6, 23]. Varactor diodes may also be used to achieve frequency-tunable behavior [6, 10, 11, 13, 23].

Generally, RF-MEMS switches provide low insertion losses, reduced power consumption, high isolation, and possibility of monolithic integration [8, 23]. However, the switching speed is relatively low, 1-200 μs [6, 23]. PIN diodes provide faster switching speed (1–100 ns) [6], but consume more DC power than RF-MEMS or FET switches [12]. Varactor diodes allow frequency-tunable responses [5, 6] and low power usage [14]. Switches only permit digital states, while varactor diodes are tunable along a continuum.

2.3 Previous Research of PIN Diode-Switched Reconfigurable Antennas

Cetiner, et al. [8] introduced RAs with a PIN-diode reconfiguration technique. A patch antenna (chosen for its unidirectional beam pattern and planar surface, thereby allowing simpler integration) is overlaid by a non-resonant pixel layer. The pixels are electrically small to be transparent to the radiated EM waves. When coupled via PIN diodes, the coupled pixels become electrically longer. According to Yagi-Uda theory, connected, longer pixels act as reflectors, whereas the disconnected, shorter pixels act as directors. Similar mathematical derivations may be found in [24].

The different configurations were designed by using a genetic algorithm (GA) to optimize the switching structure to optimize gain at specific frequencies and in certain directions. The design was limited in frequency reconfiguration (5% centered around 9 and 10 GHz), but achieved 30° beamsteering.

Towfiq, et al. [1] researched an RA operating at 5 GHz. The antenna consisted of an aperture-coupled fed patch antenna with a planar parasitic layer placed above the patch.

The upper layer of the parasitic layer contained two pixelated metal strips, where each strip contains four equal-sized pixels, each measuring 4x8 mm ($\frac{\lambda}{8}$ x $\frac{\lambda}{4}$). Each pixel was interconnected by PIN diodes. The antenna achieved beamsteering in the hemisphere corresponding to $\theta \in$ {-40°, 0°, 40°}, $\phi \in$ {0°, 45°, 90°, -45°}. The antenna achieved reconfiguring its 3 dB beamwidth, where $\theta_{3dB} \in$ {40°, 100°}, $\phi_{3dB} \in$ {45°, 90°, -45°}.

The antenna was fabricated and had an average measured gain of 8 dB. The antenna was shown to have 12 discrete modes, corresponding to different combinations of the PIN diode switches. The paper showed an efficient PIN diode layout. The binary modes permit only discrete steering directions.

Rodrigo, et al. [25] investigated an RA capable of reconfiguring its frequency, polarization, and radiation pattern. The antenna consisted of a parasitic layer of 6 × 6 pixels, with an overall size of 0.6 $\lambda\times$ 0.6 λ and 60 PIN-diode switches. The frequency varied over 25% from 2.4 to 3.0 GHz. The polarization could switch between $\hat{x}, \hat{y}$, left-handed circular polarization (LHCP), and right-handed circular polarization (RHCP). The antenna achieved beamsteering over ±30° in E and H-planes. The average gain was 4 dB, with higher-gain modes achieving 6-7 dB.

2.4 Previous Varactor-based Reconfigurable Antenna Research

Research on varactor-based RAs achieved frequency-tunable properties. Chen Q., et al. [26] attached varactor diodes to each corner of a 29 GHz rectangular patch antenna. The antenna was tuned from 23.2 to 30.2 GHz. An array was successfully created and measured.

Zhang, et al. [11] researched a pixel dome-shaped parasitic reflective surface (PRS) at 2.45 GHz. The varactor diodes were fed via bias lines that ran from the base of the antenna to vias positioned at the center of each pixel element. The pixel elements were connected by the manner of construction, providing a path to ground. In simulation, the antenna achieved beamsteering (considering symmetry) of up to $\theta = 60°, \phi \in \{0°, 360°\}$ with a 6 dB minimum gain.

King, et al. [13], [24] introduced a type of RA that allows for continuous beam steering. Varactor diodes were used as interconnecting elements, allowing steering in 1° increments.

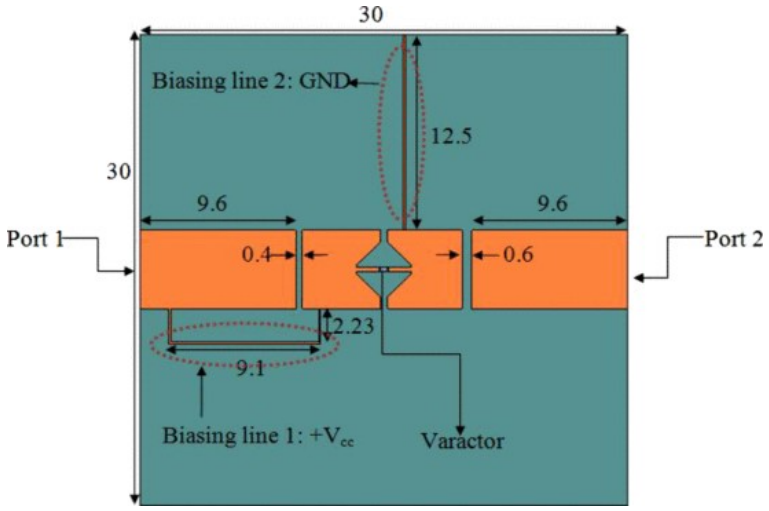

Fig. 2.3: Filtenna with biasing structure in [5] ©2012 IEEE.

The antenna was simulated in a full-wave simulator, indicating continuous beamsteering at 28 GHz over $\theta \in$ {-20°, 20°} with over 6 dB of gain. An analytical formula for the antenna radiation pattern was also derived from array principles. The pixels were modeled as patch antennas. However, the pixels do not have a nearby ground plane to create a resonator cavity as typical patch antennas do [18]. This may account for some of the discrepancy between the theoretical and simulated antenna patterns.

2.5 Varactor Biasing Networks

Y. Tawk, et al. [5] researched a varactor-based tunable filtenna. A hexagonal gap was etched into the center of a microstrip feed line. Two rectangular gaps were also etched across the microstrip line. The gaps provided a capacitance for the filter. The researchers integrated a varactor across the hexagonal gap to vary the capacitance. A bias tee was connected to one filter port to pass RF and DC control signals. A thin high-impedance bias line was then connected across a rectangular gap to allow DC control currents through. The current passed through the line to the varactor and to ground via another thin high-impedance line. See Fig. 2.3. The filter was subsequently integrated with a printed Vivaldi antenna. The varactor allowed tuning the filtenna from 6.16 to 6.6 GHz.

2.6 Dielectric Properties of 3D Printed Materials

3D printing allows rapid prototyping and manufacture of designs otherwise difficult to obtain by conventional techniques. The fabrication of the dome for the second antenna variant uses 3D printing. Three common plastics used in 3D printing are Polylactic Acid (PLA), Polyethylene Terephthalate Glycol (PET-G), and Acrylonitrile Butadiene Styrene (ABS). The plastics have magnetic, dielectric, and conductive variants. Many of the chemical and mechanical properties of PLA are given in [27].

The work [28] measured the relative permittivity of PLA with various dyes, PET-G and ABS from 1 MHz to 100 MHz. The relative permittivity varied from 2.9–4.2. The loss factor varied by 0.8–4.0%. The dyes made little difference to the relative permittivity. The work [29] measured and charted dielectric properties of magnetic, dielectric, and conductive PLA from 2-20 GHz. The results are charted in the paper. ϵ_r at 5 GHz for dielectric PLA is about $3.5 + j0.2$, although an exact number is not available from the paper.

2.7 Spherical Parasitic Layer (SPL) Antenna Fabrication

One of the novelties of this research is the use of a spherical parasitic layer explained in § 5.1. It is expected that the manufacture of the spherical layer by standard PCB techniques will be difficult. However, additive electronic manufacturing (AEM), e.g. 3D printing, is becoming mature and can be used to create spherical shapes. The integration of electronic components, e.g. PIN diodes, varactor diodes, remains a challenge. The work [30] used a 3D printer to print a dome. Indented grooves were left in the dome and filled with conductive silver epoxy. The layers were finished via a Damescene process. The conductive silver epoxy had low conductivity compared to copper, resulting in high resistive losses. The work [31] used aerosols to apply silver to the surface and electroless plating with copper to increase the conductivity. The team used lasers to etch the appropriate geometry in a copper sheet. The work [32] used a copper alloy thermal spray process to create conductive surfaces. The substrate was made of ULTEM™ 9085, which has a heat deflection temperature (HDT) of 350.4 °F [33]. The work [34] used copper tape on a PLA substrate to create a 9.4 GHz patch antenna. Copper tape was also used to form a flexible antenna in [35]. The use of

tape allows for tuning via adding and trimming tape along various dimensions.

CHAPTER 3

Methodology

3.1 Overview

The research investigates fine beamsteering of a planar pixel antenna using varactors around 5 GHz and beamsteering on a spherical pixel antenna using PIN diodes around 4.75 GHz. The beam tilt is measured as the direction of maximum realized gain. The research was conducted via simulation in Ansys High Frequency Structure Simulator (HFSS). The spherical antenna was fabricated and its return loss was compared to the simulation.

3.2 HFSS Simulation

HFSS is a 3D full-wave EM modeling software that allows modeling electromagnetic fields with varying geometries, configurations, and components. [36, 37] The first step in HFSS simulation is creating a model geometry of the device under test (DUT). The user assigns material properties for each object within the model. Variables used to describe dimensions and properties may be parameterized and systematically changed as an optimetric sweep. Optimetric sweeps allow the user to view the effects of changes to the design or to tune the design.

Ports and boundaries are used to further model the DUT. The DUT includes at least one port (or excitation) to pass signals into the model. Boundary conditions are assigned to the exterior of the model or surfaces of the model. For example, antenna models require a radiation boundary or a perfectly matched layer (PML) to measure radiated fields. Perfect conductors may also be modeled as perfect electric conductor boundaries. Lumped element boundary conditions allow simulation of Resistance-Inductance-Capacitance (RLC) circuits without an external model, such as a lumped element model for a PIN diode. Ansys Circuit models may be linked to HFSS models via *cosimulation*.

The second step in HFSS modeling is to create a setup of a solution. The user assigns a "solution frequency, desired convergence criteria, maximum number of adaptive steps to perform, frequency band over which solutions are desired, and what particular solution and frequency sweep methodology to use" [37].

The third step is model analysis. HFSS converts model geometry into tetrahedral representations, a process known as meshing. Meshing details may be automatic or manual. This research used automatic mesh sizing. Boundary conditions are applied to each mesh, and Maxwell's equations are solved for each tetrahedron throughout the model by solving corresponding matrices. The results are iterated to achieve higher accuracy. The iteration stops once a specified number of iterations is reached or a specified weighting condition is met. The result are EM fields throughout the model, in both the near- and far-fields [37].

Post-processing the results is the last step. Post-processing includes plotting results, such as S-parameters or radiation fields. HFSS allows plotting any field quantity or S, Z, or Y parameter. Extrema of graphs may be found via plotting or calculations. HFSS allows importing and exporting data as Touchstone, csv, dsp, and other file formats, based on the data type.

Multiple simulations may be run consecutively as optimetric sweeps. Two important types of optimetric sweeps are parametric sweeps and optimization sweeps. In a parametric sweep, variables are changed in a predetermined series of values. Multiple variables may be set to change simultaneously or individually. Optimization sweeps variables until a weighting criterion is met or the maximum number of iterations is completed. Optimization sweeps allow tuning the model to singular or multiple desired criteria.

3.3 Procedure

The research may be divided into two parts. The first part fulfills the first three objectives; namely:

1) Demonstrate the utility of varactor diodes for antenna beamsteering using planar parasitic layer-based RAs.

2) Demonstrate the utility of varactors diodes for sub-6 GHz RAs.

3) Demonstrate fine beam steering using varactors diodes on a planar parasitic layer for RAs.

The second part fulfills the last objective:

4) Demonstrate a wider beam steering range (i.e., wider field of view) using PIN diodes in spherical shaped parasitic layer-based RAs as opposed to a planar parasitic layer-based RA.

3.4 Part 1: Varactor Diodes on Planar Parasitic Layer

The first step simulates the antenna described and studied in [1]. This antenna is a baseline to compare beamsteering angles and gain patterns. Simulations were expected to produce results similar to those described in [1]. See results in Section 4.1.

The second place replaces the PIN diodes with varactors, initially modeled as variable capacitors. The capacitance was varied via optimetric sweep. The antenna's reflection loss, realized gain, and beam steering angles were compared to that of the PIN diode antenna found in [1].

The third step was iterating the design with a more complete model of a varactor, such as an S-parameter file from a vendor or a lumped-element RLC circuit model. The antenna design was optimized for larger beam tilt and gain. Parametric sweeps across capacitance values allowed visualization of the large search space. Radiation and return loss plots (with corresponding tables) were created for the most effective modes.

These simulations fulfilled the first three objectives.

3.5 Part 2: PIN Diodes on Spherical Parasitic Layer

The first step of the research into the SPL was building the spherical layer and antenna in HFSS. See § 5.1.1. The antenna used copper strips to simulate an idealized antenna's behavior. The second step replaced the copper strips with pixels and PIN diodes. The third step optimized gain and beamsteering using HFSS optimetrics by sweeping the pixel size and geometry. The fourth step added bias lines and biasing network components. This biasing network was based on the one in [1]. The fifth step was simulating the antenna

again with the bias lines and biasing network to ensure minimal effects on the antenna's radiation pattern. Fabrication considerations were incorporated into the model without the bias circuitry. The beamsteering capability, return loss, and gain were measured for the both the simulated fabricated antenna and the full biasing network circuitry. These measurements fulfill the last objective.

An additional step was spherical antenna fabrication and measurement. The bottom layers follow typical PCB construction and used gerber files. The spherical parasitic layer was 3D-printed and used stl files. The dome was printed using PLA filament. The antenna PCB and parasitic layer were connected via nylon screws. Copper tape was used to create the pixels and approximate PIN diodes using short circuits. The following step was testing the return loss (RL) using a calibrated Anritsu MS4640B Vector Network Analyzer (VNA). The simulations and measurements were plotted and compared.

3.6 Expected Results

It was expected that varying the capacitance of the varactors would allow continuous beamsteering. However, the antenna was not expected to beam steer into large angles away from boresight. This arises from the operating theory of the antenna. The antenna consists of an array of antennas that follow the Yagi-Uda principle, where one driven element drives the parasitic layers. All the antennas radiate primarily in the $\hat{z}$-direction, and the contributions at large angles away from the $\hat{z}$-direction is minimal. It was expected that lower capacitance values would have reduced impedance and consequently, coupling between adjacent pixels would increase. Increasing coupling would have made the pixels behave as reflectors in Yagi-Uda theory, and hence steer the beam away from the pixels with lower coupling. See [24] for a more analytical explanation. An expected problem are large sidelobes and a large beamwidth (due to the usage of patch antennas).

A spherical parasitic layer is expected to have improved coupling to the radiated field from the driven patch antenna. This arises from the near-spherical phase front in the near-field of a patch antenna [4]. As a result, the maximum beamsteering angle and gain is expected to be greater than the planar parasitic layer.

CHAPTER 4

Results and Model Construction of the Planar Parasitic Layer (PPL) Reconfigurable Antenna (RA)

4.1 Baseline PPL Model

The first step was to create a baseline model by recreating and simulating the PPL RA designed in [1] in HFSS. The antenna was constructed as far as the description in [1] allows. The antenna was simulated and excited at 5 GHz. The model used a vacuum-filled radiation box. However, the model did not yield the expected results. The return loss (RL) was initially found to be about 6 dB. The antenna stub and aperture length dimensions were tuned to minimize RL. The PRS was also removed to minimize RL. The RL was thus improved to 15 dB. The height of the parasitic layer was tuned to improve beamsteering capability and antenna gain. The height was parametrically swept in increments of 2 mm and the original height (6, 6.59, 8, 10, 12, 14, 16 mm). RL increased with height and beamsteering angle decreased. 8 mm was chosen to jointly optimize RL and maximum beamsteering angle. The final dimensions for the antenna are shown in Fig. 4.2 and Table 4.1. To denote the switching elements (PIN diodes, varactors), either numbers or right and left sides are used. Right refers to the $+x$ direction, whereas left refers to the $-x$ direction. Using the same orientation, each switching element may be numbered from the left, uppermost diode, then down the left side, then from the right, the uppermost diode down, as seen in Fig. 4.1. Each switching element is modeled as an appropriate lumped Resistance-Inductance-Capacitance (RLC) boundary. The values and series-parallel configuration are explained in more detail with each model.

The antenna was initially simulated using perfect open (i.e., no connector) and short (i.e., copper strip) connections between the pixels to simulate ON- and OFF-states in PIN diodes as seen in Fig. 4.3. As expected, the results of the model resembled those given

Table 4.1: Planar Parasitic Layer Reconfigurable Antenna (PPL RA) Dimensions as seen in Fig. 4.2.

Dimension Abbreviation	Dimension Name	Quantity (mm)
SA_x	Substrate Length	61.0
SB_y	Substrate Width	61.0
DAh	Substrate Height	3.0
Sx	Parasitic Substrate Length	61.0
Sy	Parasitic Substrate Width	67.0
DAh	Parasitic Substrate Height	3.0
M_y	Feedline Length	31.8
W_x	Feedline Width	1.8
-	Stub Length	2.8
FLh	Feed Height	0.8
A_x	Aperture Length	9.4
A_y	Aperture Width	0.8
P_x	Antenna Length	12.5
P_y	Antenna Width	12.7
SP_y	Pixel Length	6.0
SP_x	Pixel Width	4.0
$\frac{D_y - 3 \cdot SP_x}{3}$	Gap between Pixels	3.0
D_x	Pixel Offset	18.0
-	Copper Thickness	0.017

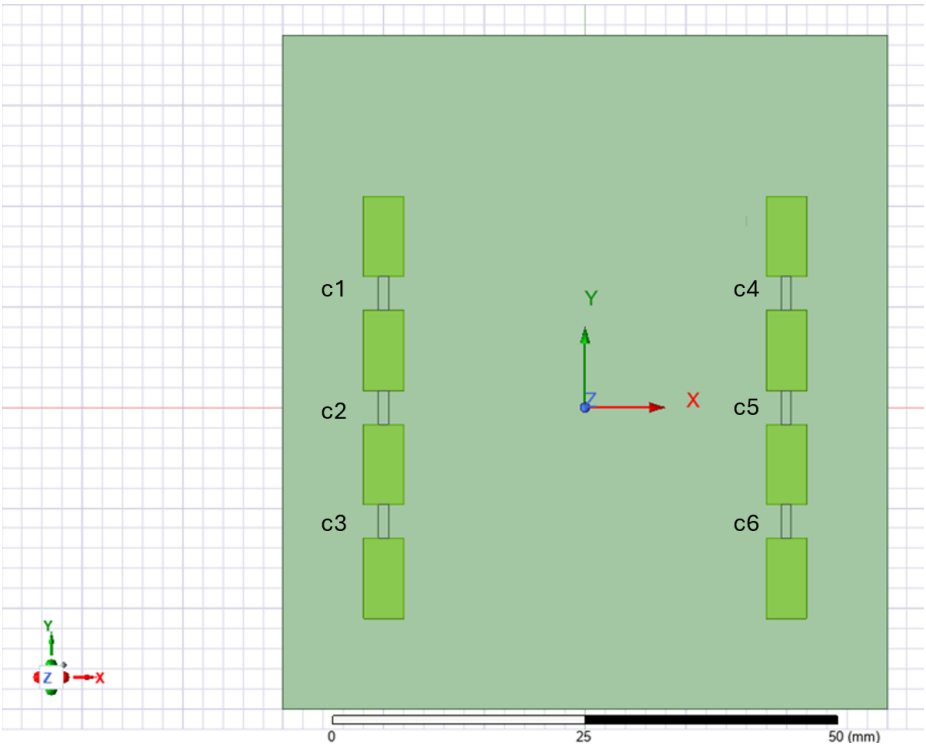

Fig. 4.1: Varactor diode nomenclature on PPL

in [1]. See figs. 4.4 to 4.6. The maximum beam tilt achieved in the new model is $\theta = 38°$; $\phi = 0°$ with a gain of 7.8 dB. This mode (Modes 1, 3) is achieved with the right-side diodes ON and the left-side diodes OFF, or vice versa. Towfiq et al. achieved 40° beamsteering with ∼8 dB realized gain [1]. The differences may arise from antenna geometry differences, particularly the parasitic layer height (8 mm vs. 6.59 mm).

A cosimulation between the antenna in HFSS and Ansys Circuit was also conducted. The MA4AGFCP910 PIN diode was used, modeled by the S-parameter file (.s2p) given on its datasheet [38]. The diodes were connected to the antenna via lumped ports. The two results were essentially identical.

4.2 Varactor PPL Model

The same antenna was used for modeling with varactors by replacing the PIN diodes with varactors. The results are shown in § 4.3. A capacitance range from 0.32 pF to 3.2 pF was used, based on the Skyworks SMV2020-079LF. This capacitor has the largest

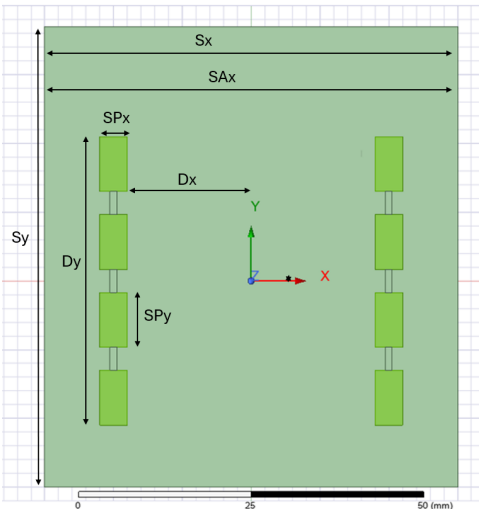

(a) Planar antenna with dimensions seen from $+z$ direction

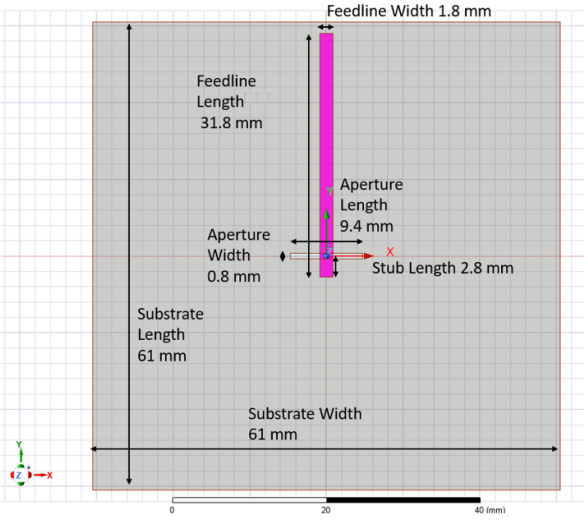

(b) Internal components of planar antenna seen from $+z$ direction

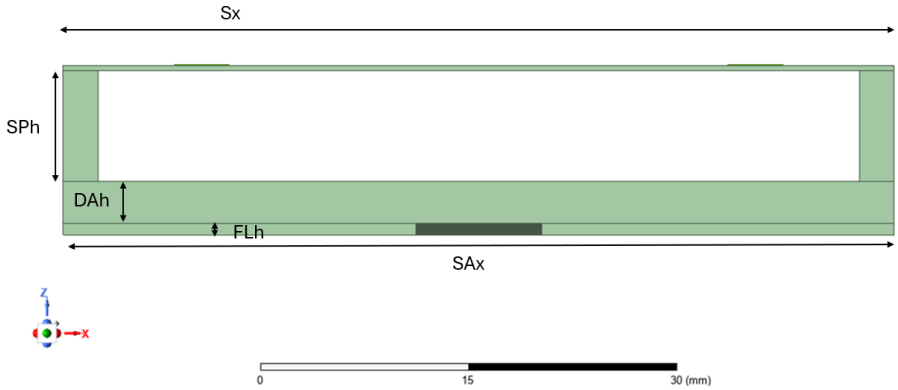

(c) Planar antenna with dimensions seen from $+x$ direction

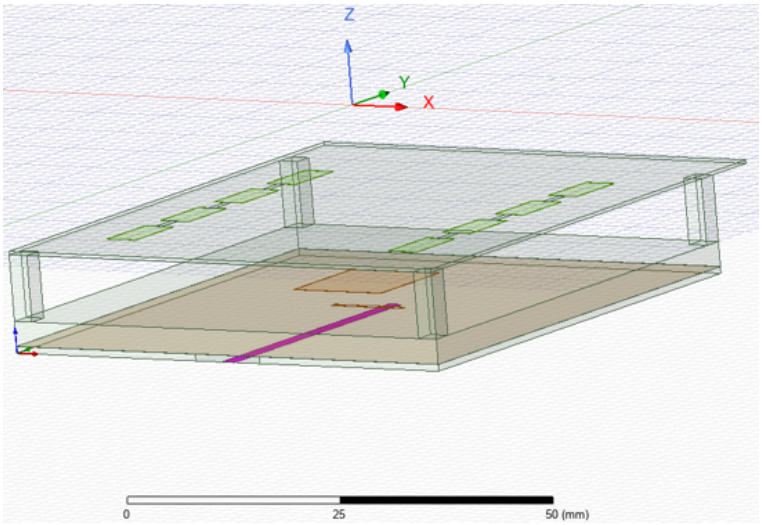

(d) Internal components of planar antenna seen from a skew direction

Fig. 4.2: Planar Antenna Dimensions listed in Table 4.1

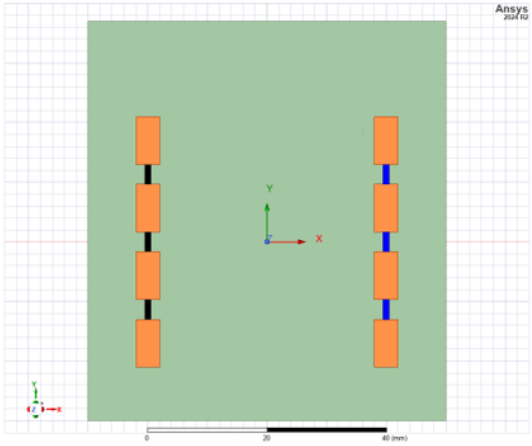

(a) Left OFF, Right ON

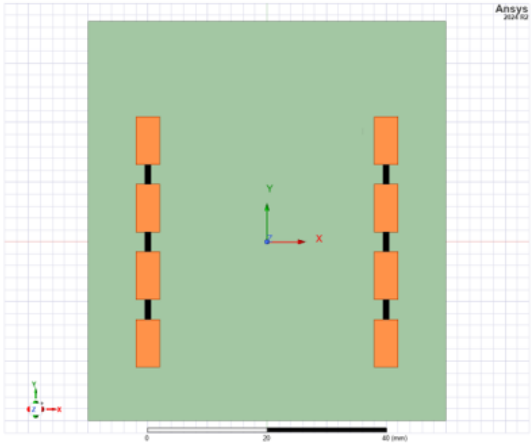

(b) Left OFF, Right OFF

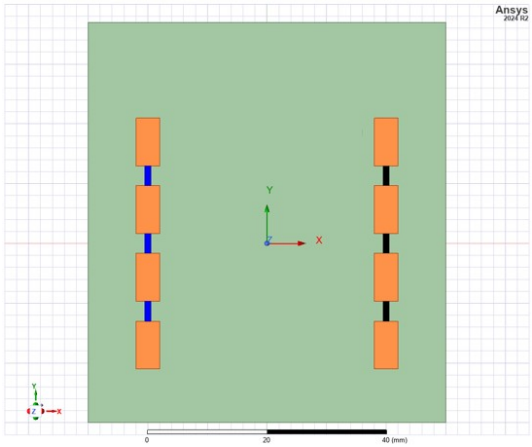

(c) Left ON, Right OFF

Fig. 4.3: Perfect Open/Short Antenna Baseline Model. ON states are denoted as blue rectangles, OFF states are denoted as black rectangles.

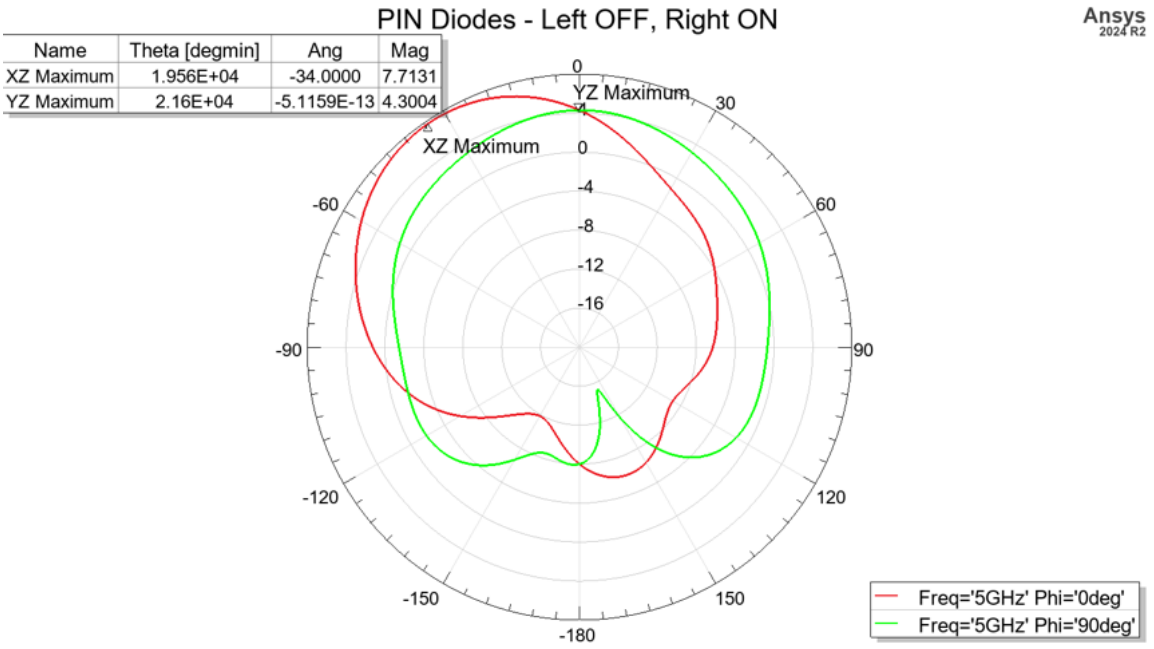

(a) Left OFF, Right ON Radiation Pattern

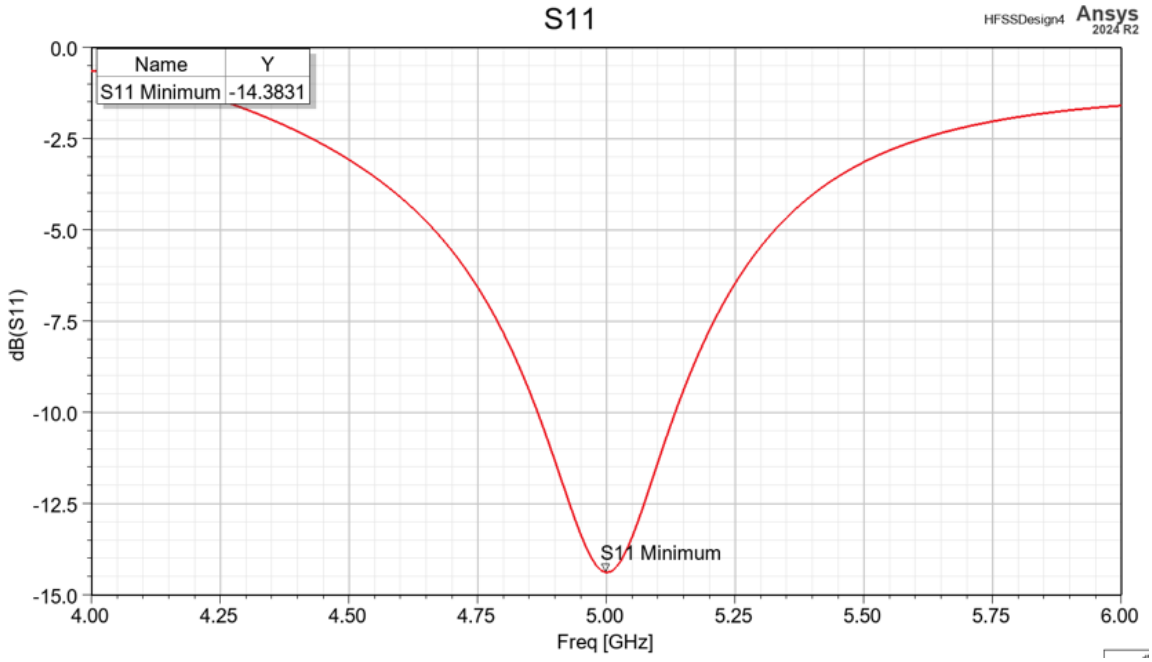

(b) Left OFF, Right ON S11

Fig. 4.4: Perfect Open/Short Antenna Baseline Model Results, Part 1

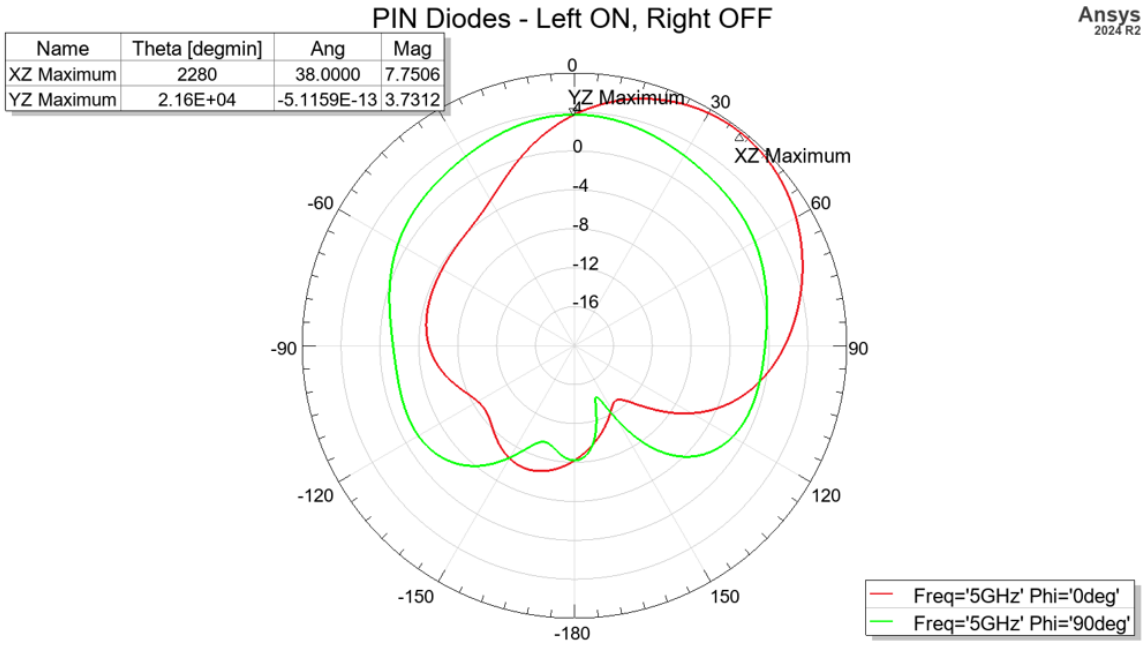

(a) Left ON, Right OFF Radiation Pattern

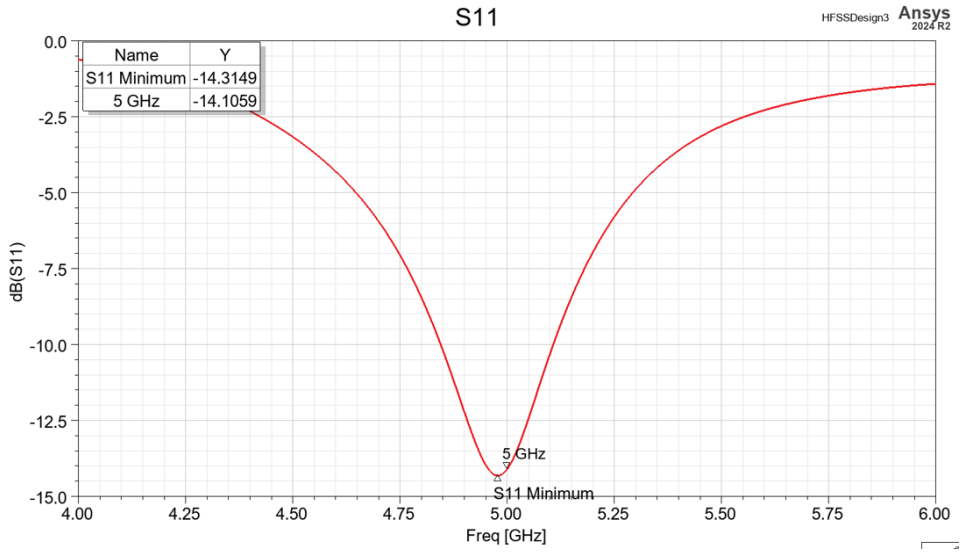

(b) Left ON, Right OFF S11

Fig. 4.5: Perfect Open/Short Antenna Baseline Model Results, Part 2

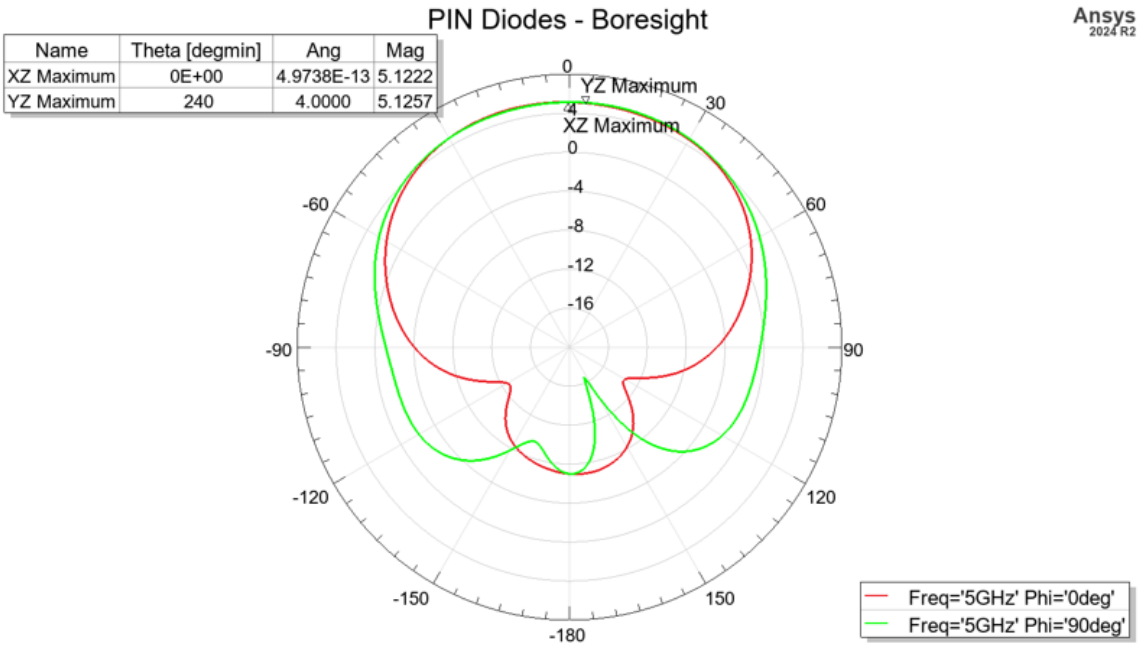

(a) Boresight Radiation Pattern

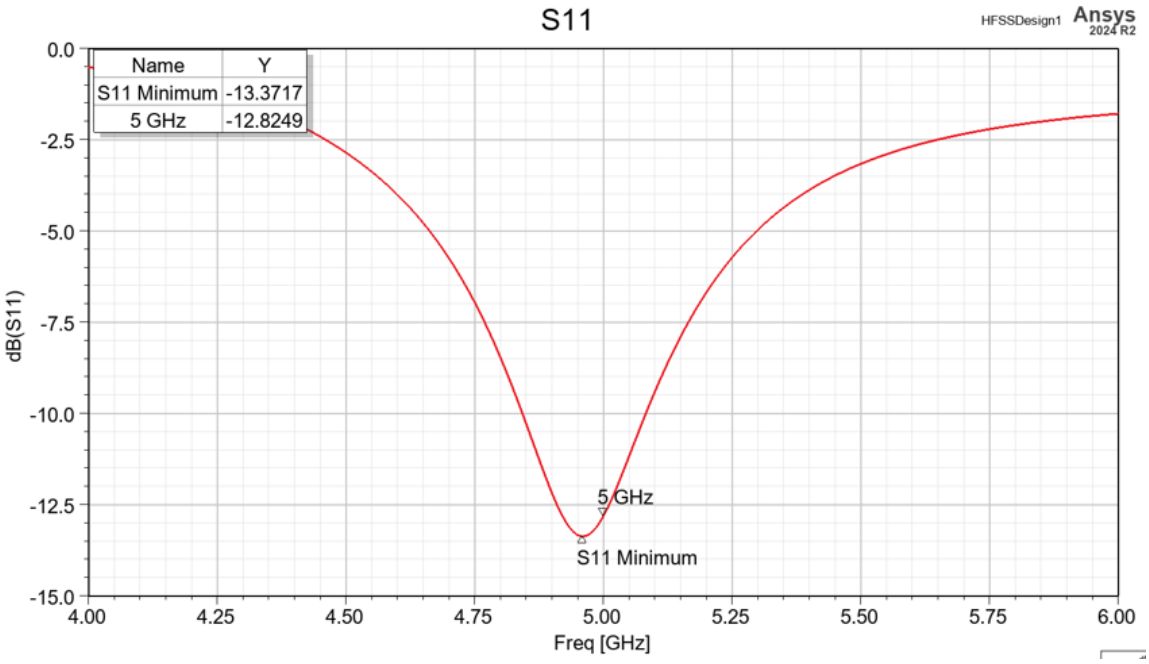

(b) Boresight S11

Fig. 4.6: Perfect Open/Short Antenna Baseline Model Results, Part 3

capacitance range of the examined varactors. The capacitance range in this varactor is created by varying the reverse bias voltage from 0 to 20 V [39]. The full Spice model is given in [39]. The model contains an inductance (0.7 nH) in series with a capacitor (0.32-3.2 pF) and resistor (2.5 Ω) in parallel. Plots and equations relating the capacitance and reverse voltage to the gain and beamsteering angle are given in § 4.4.

The varactor diode was implemented as a capacitor because the other Spice-model parameters describe the voltage - capacitance curve, which was not needed to demonstrate beamsteering. As previously mentioned, the varactor model was implemented as an RLC lumped element boundary condition between pixels. No biasing network was created for this antenna. Practically, a DC blocking capacitor could be used to separate varactor bias voltages or the series voltages across the diodes would need to be accounted for by a controller. The capacitance from a biasing network would need to be taken into account, likely by lengthening the pixels and choosing a different varactor.

4.3 Varactor Modes

Three major simulation campaigns were run on the varactor-based PPL RA. Modes with beamsteering primarily in the xz-plane are shown in § 4.3.1. Campaign A is explained in § 4.3.2 and is primarily boresight modes. Campaign B is explained in § 4.3.3 and is primarily beamsteering in the yz-plane.

Table 4.2: Varactor xz-Plane Steering Modes

Mode Number	Left Varactor Capacitance Value (pF)	Right Varactor Capacitance Value (pF)	Plot	Table	Page
0	3.2	3.2	4.7	4.3	26
1	3.2	Swept	4.8	4.4	27
2	Swept	3.2	4.9	4.5	28
3	0.32	Swept	4.10	4.6	29
4	Swept	0.32	4.11	4.7	31

4.3.1 Varactor xz-Plane Modes

The modes for steering in the xz-plane are listed in Table 4.2.

Mode 0 set all the varactors at 3.2 pF. This is the maximal gain boresight mode. The results are shown in Fig. 4.7 and Table 4.3 on page 26.

Mode 1 set the left side varactors (C1-C3) at 3.2 pF, while sweeping the values of the right side varactors (C4-C6). The results are shown in Fig. 4.8 and Table 4.4 on page 27.

Mode 2 is the opposite of Mode 1. Mode 2 swept the value of the left side varactors (C1-C3), while setting the values of the right side varactors (c4-c6) at 3.2 pF. The results are shown in Fig. 4.9 and Table 4.5 on page 28.

Mode 3 set the left side varactors C1-C3) at 0.32 pF, while sweeping the values of the right side varactors (c4-c6). The results are shown in Fig. 4.10 and Table 4.6 on page 29.

Mode 4 is the opposite of Mode 3. Mode 4 swept the value of the left side varactors (C1-C3), while setting the values of the right side varactors (c4-c6) at 0.32 pF. The results are shown in Fig. 4.11 and Table 4.7 on page 31.

Modes 1 and 2 demonstrate fine beamsteering from $\theta \in \{23°, -23°\}$, $\phi = 0°$. The largest rate in beam steering vs. capacitance occurs when the right capacitor values vary between 0.32 and 1.14 pF and the left capacitance values are set at 3.2 pF (or vice versa) over the angle $\theta \in \{\sim \pm 10°, \sim \pm 23°\}$. It was expected that decreasing the capacitance value between pixels would increase impedance between the pixels, thus decreasing coupling, thus creating electrically shorter pixels, and steering the beam in the direction of least capacitance. Surprisingly, the beamsteering occurred in the opposite direction. This result is expected to be caused by current leading voltage by 90° or $\frac{\lambda}{4}$ in capacitors. The parasitic

Table 4.3: Mode 0, Boresight: All Varactor Capacitance Values set at 3.2 pF. Note the symmetry around the $\hat{z}$-axis.

Right Varactor Capacitance Value (pF)	Realized Gain (dB)	Beamsteering Angle (°)
3.2	5.20	0.1

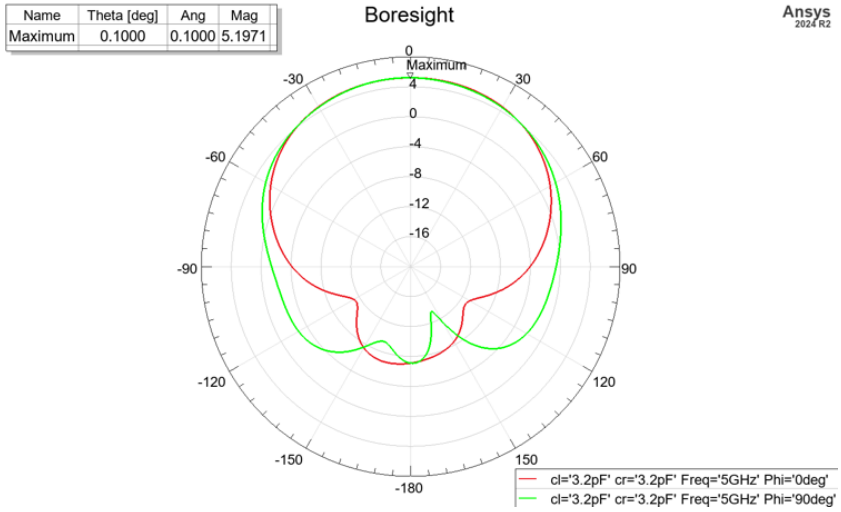

(a) Boresight Radiation Pattern, xz- and yz-Planes

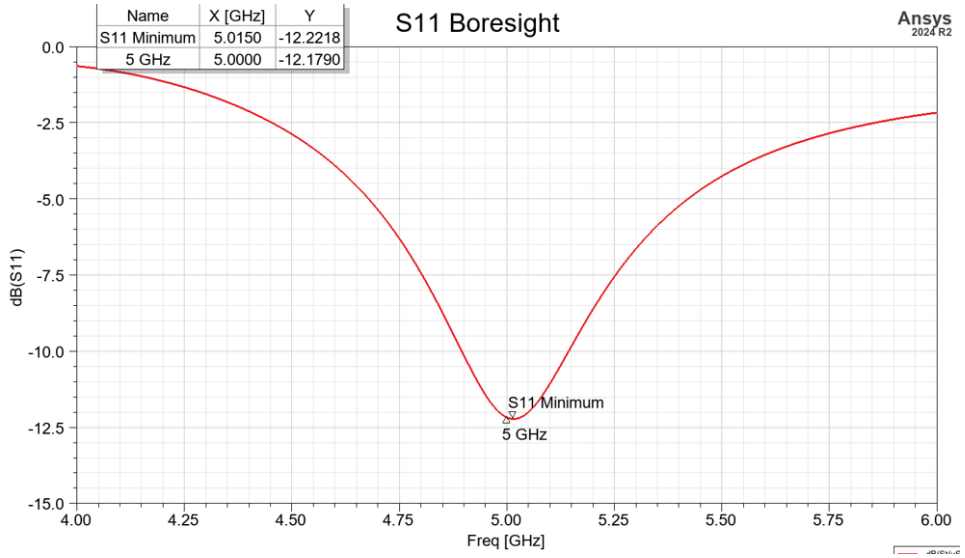

(b) S11

Fig. 4.7: Mode 0, Boresight: All Varactor Capacitance Values set at 3.2 pF

Table 4.4: Mode 1 Results, xz-Plane: Sweep Right Values, Left Values = 3.2 pF

Right Varactor Capacitance Value (pF)	Realized Gain (dB)	Beamsteering Angle (°)
0.32	5.13	-23.0
0.73	5.15	-15.0
1.14	5.15	-7.6
1.55	5.11	-6.1
1.97	5.20	-0.1
2.38	5.21	-1.7
2.79	5.17	0.2
3.2	5.20	0.1

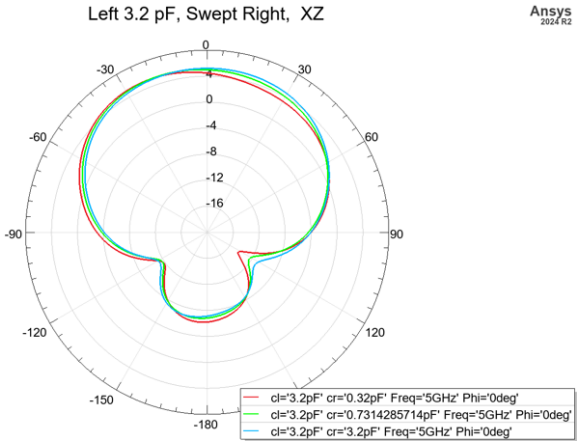

(a) xz-Plane

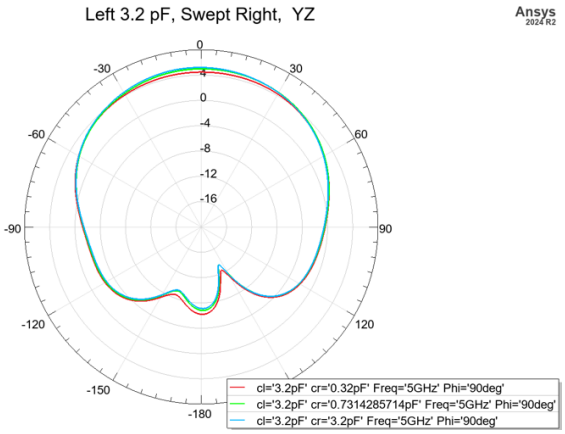

(b) yz-Plane

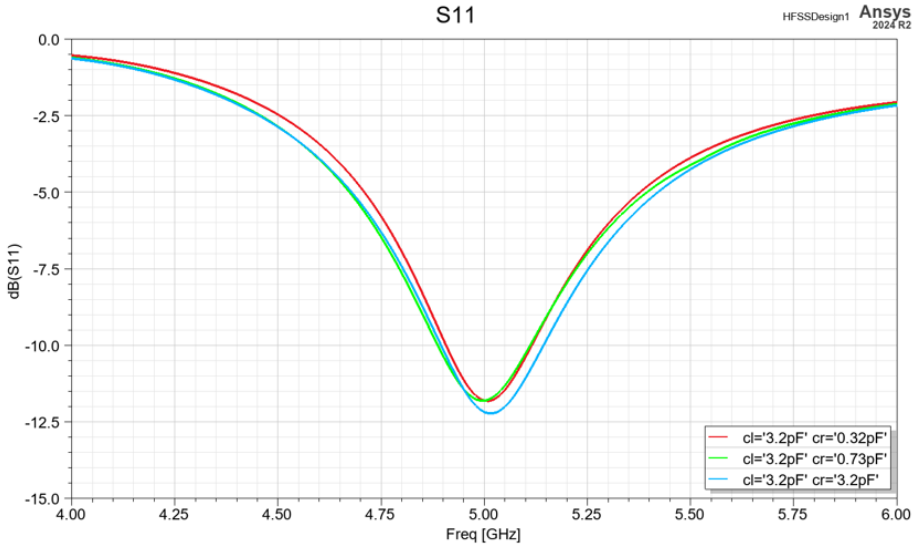

(c) S11

Fig. 4.8: Mode 1: Sweep Right Values, Hold Left Values at 3.2 pF

Table 4.5: Mode 2: Sweep Left Values, Hold Right Values at 3.2 pF

Right Varactor Capacitance Value (pF)	Realized Gain (dB)	Beamsteering Angle (°)
0.32	5.13	23.0
0.73	5.15	14.1
1.14	5.12	10.0
1.55	5.16	6.7
1.97	5.20	4.7
2.38	5.21	3.5
2.79	5.19	0.4
3.2	5.20	0.1

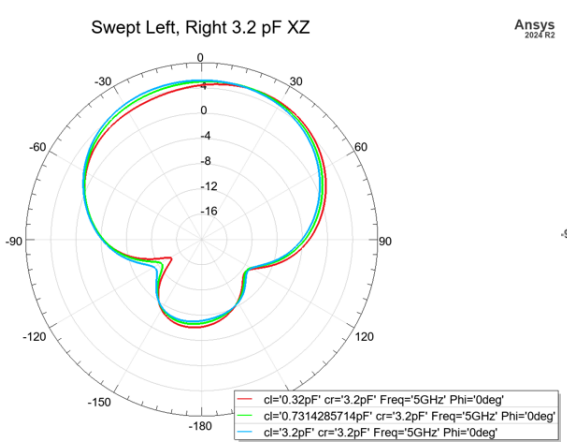

(a) xz-Plane

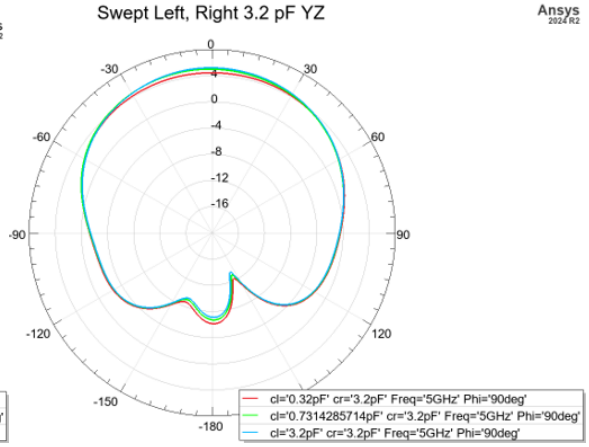

(b) yz-Plane

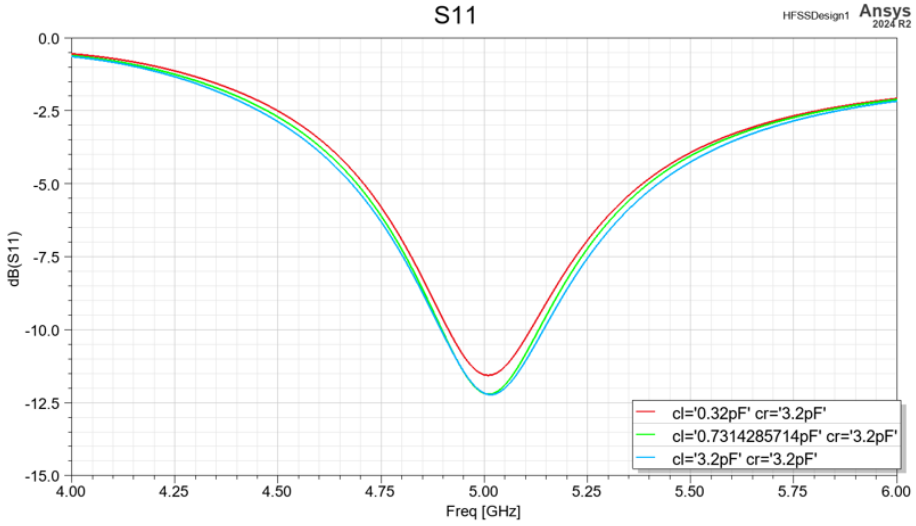

(c) S11

Fig. 4.9: Mode 2: Sweep Left Values, Right Values = 3.2 pF

Table 4.6: Mode 3: Sweep Right Values, Hold Left Values at 0.32 pF

Right Varactor Capacitance Value (pF)	Realized Gain (dB)	Beamsteering Angle (°)
0.32	3.81	0.4
0.73	4.65	20
1.14	4.93	21.3
1.55	5.00	21.3
1.97	5.11	22.4
2.38	5.13	22.2
2.79	5.20	22.7
3.2	5.11	22.1

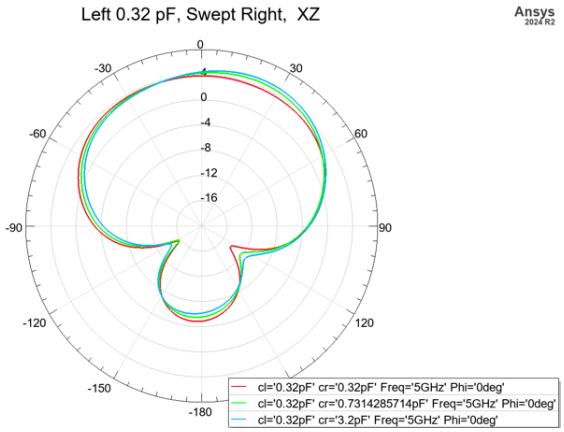

(a) xz-Plane

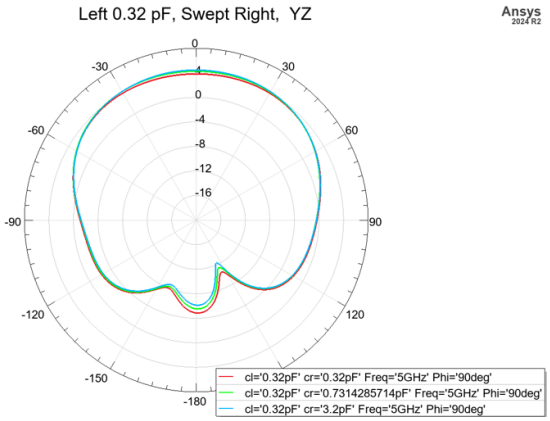

(b) yz-Plane

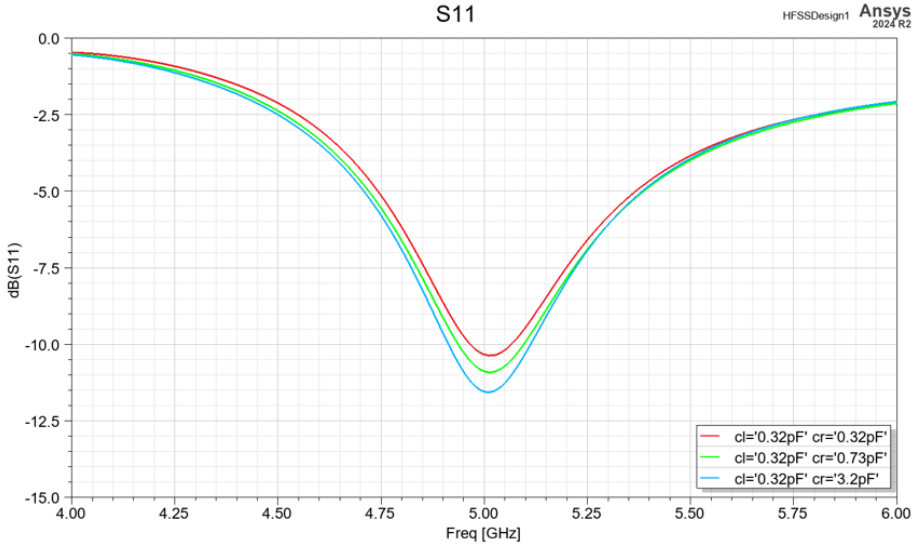

(c) S11

Fig. 4.10: Mode 3: Sweep Right Values, Hold Left Values at 0.32 pF

inductances and resistances change the realized overall phase shift across the varactor diode. The phase shift creates an overall electrical shortening (opposite the effect of loading coils for sub-UHF antennas) and changes the interference pattern created by the Yagi-Uda effect. The increased capacitance also increases the resonant frequency of the pixels, in similar fashion to [26].The simulations indicate that the antenna is capable of fine beamsteering from $\theta \in \{\sim \pm 23°, 0°\}, \phi = 0°$.

4.3.2 Varactor Campaign A

Campaign A swept the middle pixels while holding the outer varactors constant. The maximum steering was $\theta = 3.9°$ on the $\phi = 0°$ plane, and $\theta = -23.9°$ on the $\phi = 90°$. However, the beam is described more accurately as a very wide beam in the boresight direction with slight variations. See Fig. 4.13 and Table 4.12 on page 32.

4.3.3 Varactor yz-Plane Modes

Campaign B was designed to test beamsteering in the yz-plane. Varactors mirrored across the y-axis were held at the same value, but were varied along the y-axis. For example, C1 and C4 were held at the same value (known as C14). Likewise for C2 and C5 (C25) and C3 and C6 (C36). Because the antenna is symmetric across the xz-plane above the ground plane, switching the values of C14 and C36 also switches the sign of the elevation angle θ. See figs. 4.14 to 4.17.

Generally, each plot will have one varactor capacitance varied through 8 values. Each capacitance value generates a separate radiation pattern on the plot. The maximum gain position on each radiation pattern is recorded in corresponding tables 4.9 to 4.22.

Each plot has markers at maximum gain points (MGP) for the corresponding swept capacitance values. The beamsteering trends are clear from the plot, although markers have been removed for legibility. Each marker is assigned a letter, a-i. The scale (Table 4.8) maps which value each letter represents. For example, if a plot has a letter b at -5°, and the plot is uses Scale 2, indicating 0.39 pF for C14 produces a MGP at -5°. The exact angle and gain can be looked up in the corresponding table.

Table 4.7: Mode 4: Sweep Left Values, Hold Right Values at 0.32 pF

Right Varactor Capacitance Value (pF)	Realized Gain (dB)	Beamsteering Angle (°)
0.32	3.81	0.4
0.73	4.62	-20.1
1.14	4.85	-21.4
1.55	4.94	-22.5
1.97	5.01	-22.9
2.38	5.07	-22.8
2.79	5.09	-22.9
3.2	5.13	-23.0

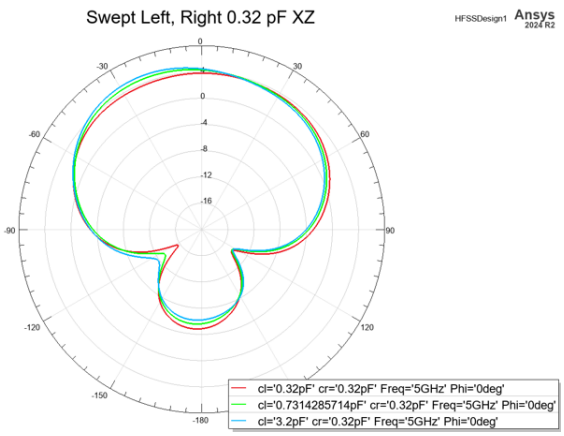

(a) xz-Plane

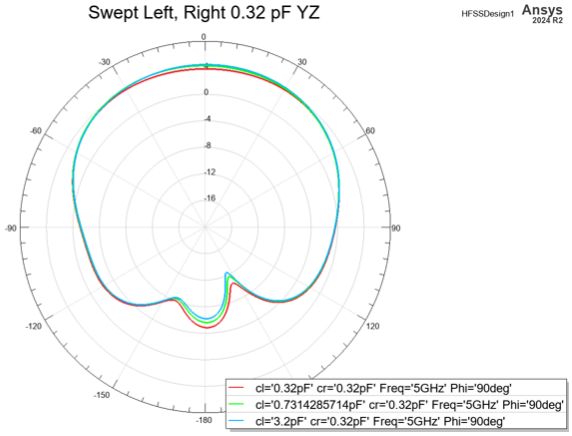

(b) yz-Plane

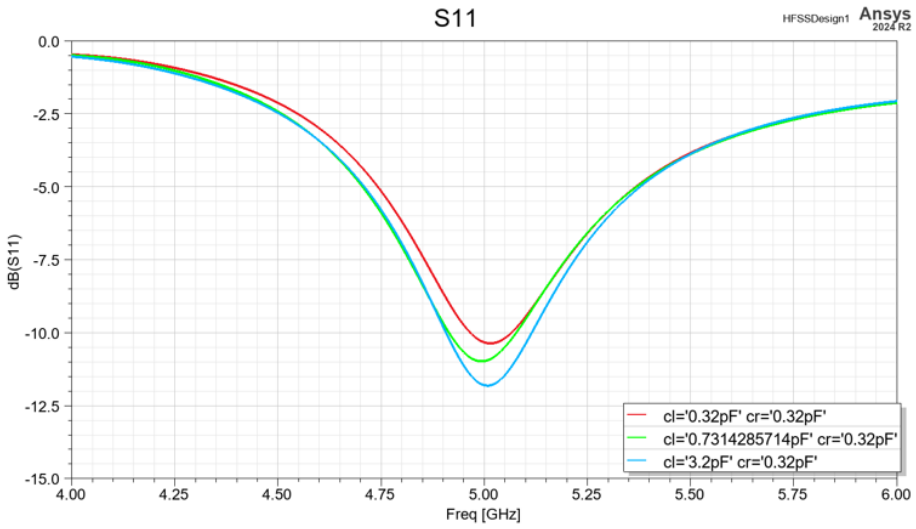

(c) S11

Fig. 4.11: Mode 4: Sweep Left Values, Hold Right Values at 0.32 pF

Fig. 4.12: Campaign A: Selected Values

Plane	Outer Capacitance (pF)	Inner Capacitance (pF)	Realized Gain (dB)	Beamsteering
xz-Plane	0.32	0.32	3.8	0.5°
	0.32	0.73	4.4	3.9°
	3.2	3.2	5.2	0.2°
	2.79	3.2	5.2	0.2°
yz-Plane	0.32	0.32	3.9	23.9°
	0.32	0.73	4.4	-14.1°
	3.2	3.2	5.2	-3.4 °
	2.79	3.2	5.2	-2.0 °

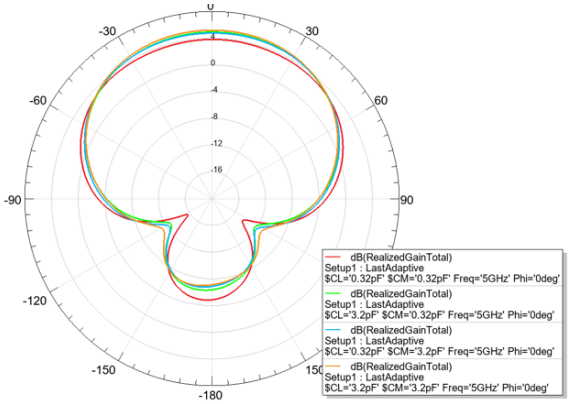

(a) xz-Plane

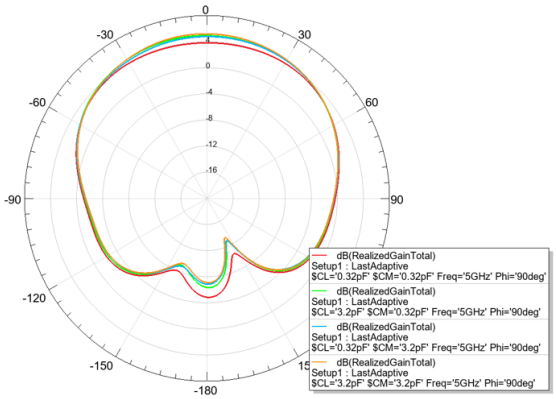

(b) yz-Plane

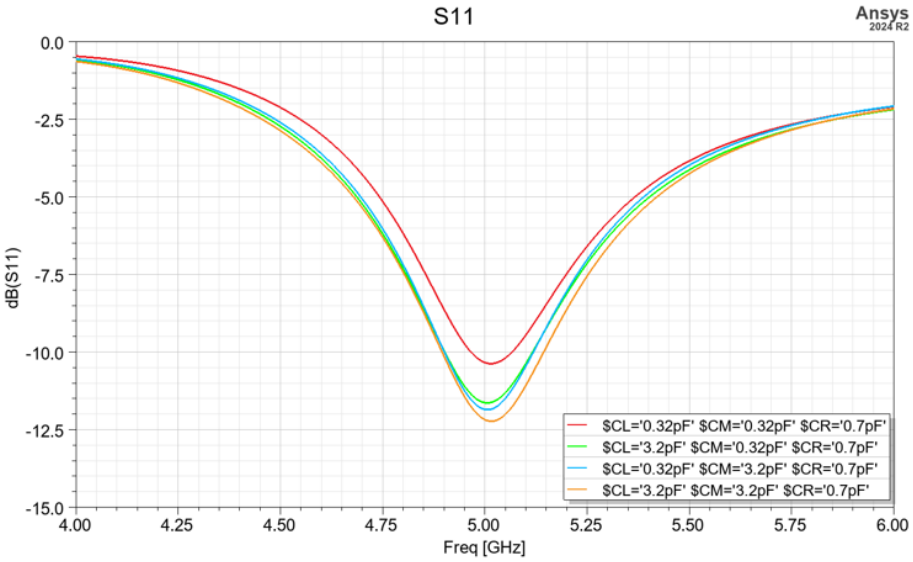

(c) S11

Fig. 4.13: Campaign A Plots. More detailed selected values are shown in Table 4.12.

Several plots were omitted for clarity, so only selected MGP are shown on the plot, with the other values shown in tables 4.9 to 4.22. However, the positions that were not marked lie between letters on either side. For example, in Plot 4.14a, only letters a, b, and i were used. Letters c-h were omitted due to lack of space. The angle for each of these values was essentially constant, with an increase in gain for each value. Each value may be seen in the tables linked to the figures.

As seen from the figures and tables, the varactor-based RA achieved fine beamsteering between $\theta \in \{-23^\circ, 23^\circ\}; \phi = 0^\circ$ (xz-plane) (Tables 4.4 and 4.5), and $\theta \in \{-25^\circ, 25^\circ\}; \phi = 90^\circ$ (yz-plane). See Figs. 4.16b. Note the fine beamsteering in Fig. 4.12, 4.14, 4.16, 4.21, 4.22. The degree to which the antenna can be steered can be as accurate as the voltage controller and manufacturing tolerances allow.

Letter	Scale 1	Scale 2	Scale 3	Scale 4	Scale 5
a	0.32	0.32	0.32	0.32	0.32
b	0.73	0.39	0.39	0.42	0.38
c	1.14	0.46	0.4	0.51	0.41
d	1.55	0.53	0.5	0.61	0.51
e	1.97	0.59	0.6	0.71	0.61
f	2.38	0.66	0.73	0.81	0.67
g	2.79	0.73	0.8	0.90	-
h	3.2	0.8	0.9	1.0	0.73
i	-	3.2	1.0	-	0.8

Table 4.8: Scales for mapping MGP capacitance values on radiation plots.

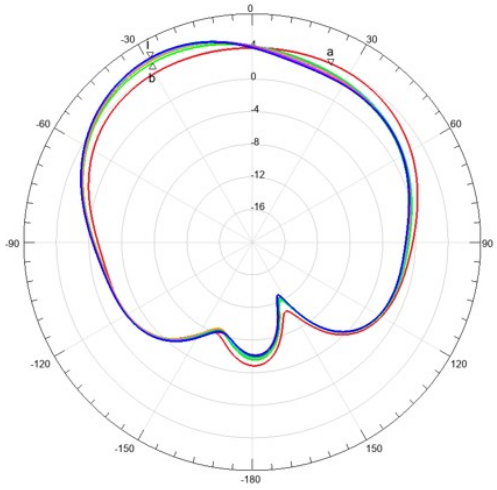

(a) Coursely Vary C14, C25 = C36 = 0.32 pF, Scale 1, Table 4.9

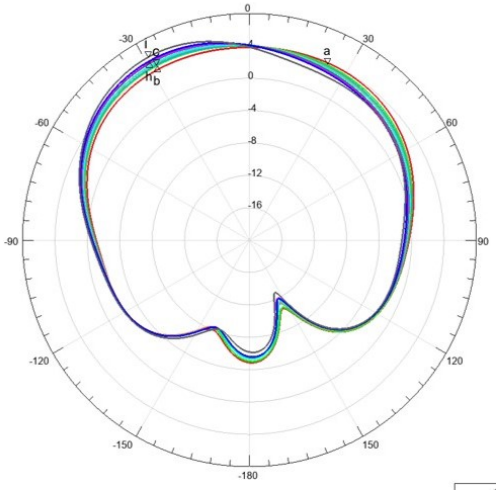

(b) Finely Vary C14, C25 = C36 = 0.32 pF, Scale 2, Table 4.10

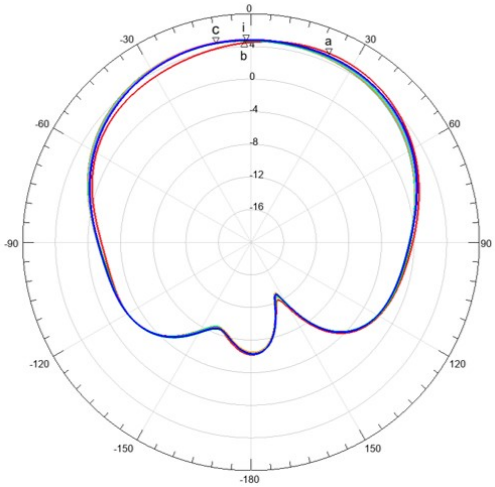

(c) Coursely Vary C14, C25 = C36 = 0.73 pF, Scale 1, Table 4.11

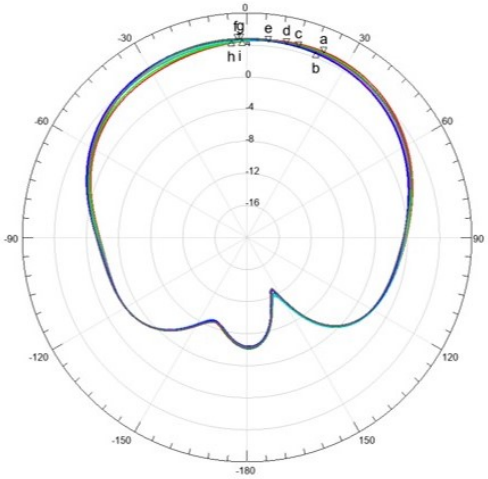

(d) Finely Vary C14, C25 = C36 = 0.73 pF, Scale 2, Table 4.12

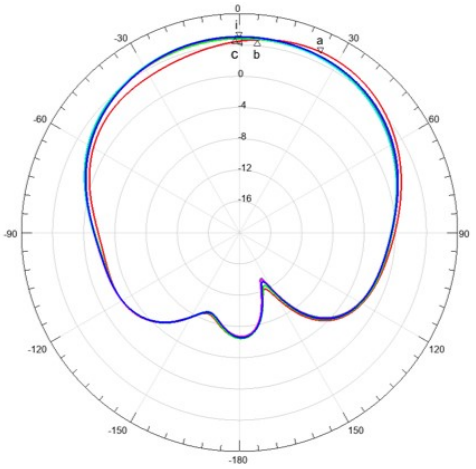

(e) Coursely Vary C14, C25 = C36 = 1.14 pF, Scale 1, Table 4.13

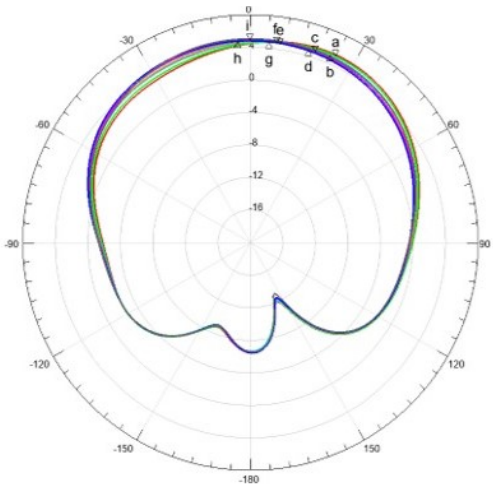

(f) Finely Vary C14, C25 = C36 = 1.14 pF, Scale 2, Table 4.14

Fig. 4.14: Campaign B: Part 1, where C25 = C36, yz-Plane, Page 1

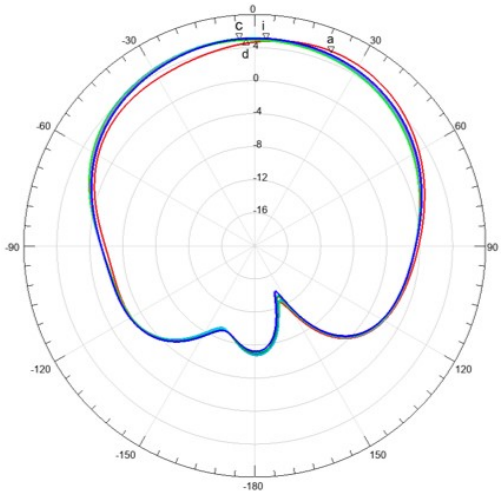

(a) Coursely Vary C14, C25 = C36 = 1.97 pF, Scale 1, Table 4.15

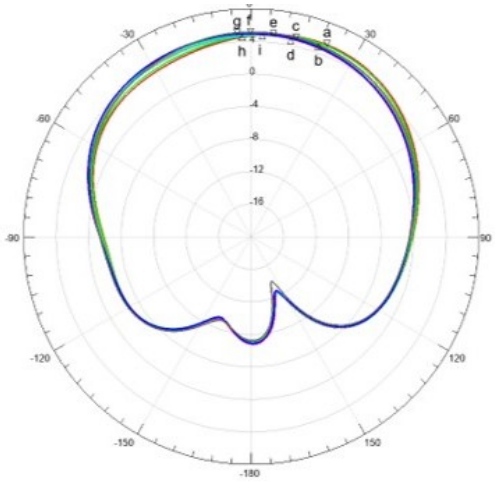

(b) Finely Vary C14, C25 = C36 = 1.96 pF, Scale 2, Table 4.16

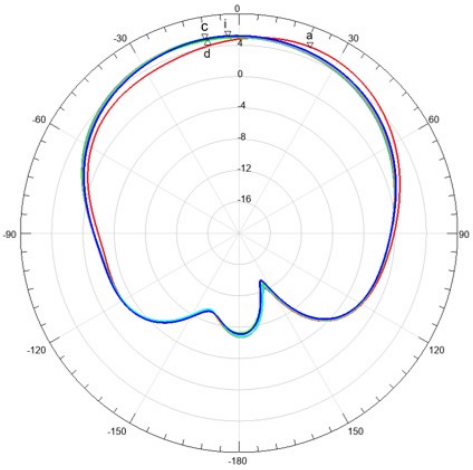

(c) Coursely Vary C14, C25 = C36 = 3.2 pF, Scale 1, Table 4.17

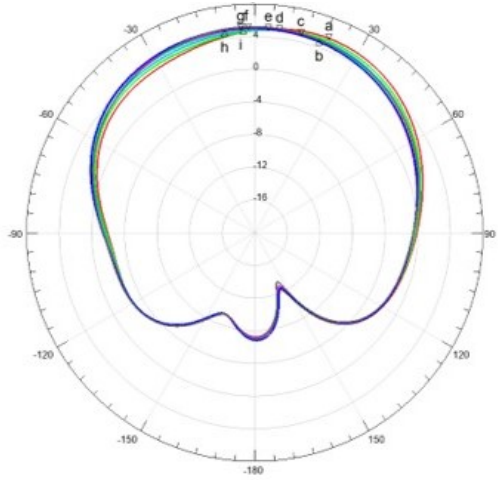

(d) Finely Vary C14, C25 = C36 = 3.2 pF, Scale 2 Table 4.18

Fig. 4.15: Campaign B: Part 1, where C25 = C36, yz-Plane, Page 2

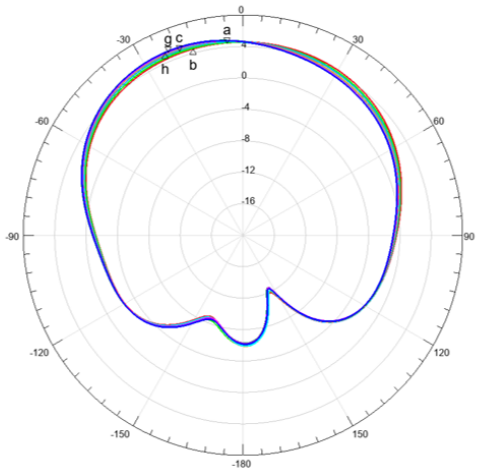

(a) Finely Vary C14, C25 = 1.0 pF, C36 = 0.32 pF, Scale 3, Table 4.19

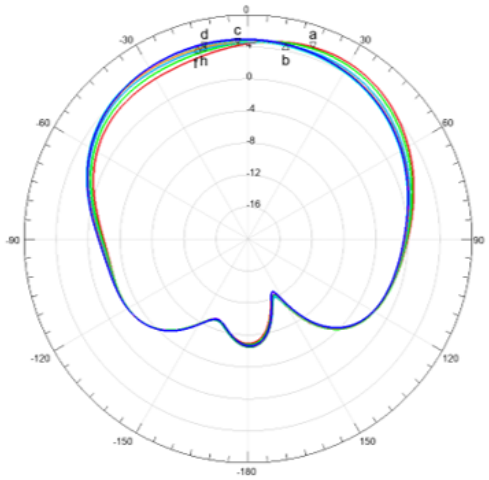

(b) Finely Vary C14, C25 = 1.0 pF; C36 = 2.0 pF, Scale 3, Table 4.20

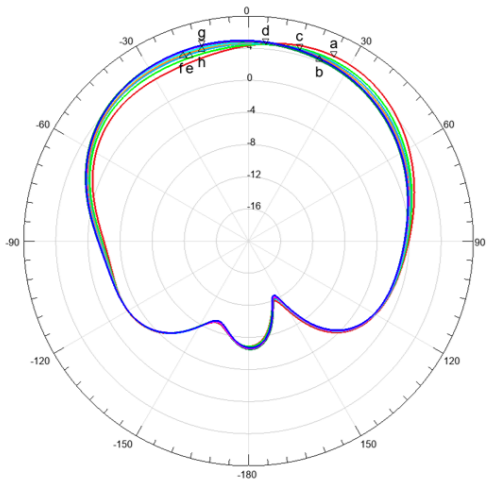

(c) Finely Vary C14, C25 = 1.0 pF; C36 = 3.2 pF, Scale 3, Table 4.21

Fig. 4.16: Campaign B: Part 2, where C25 = 1.0 pF

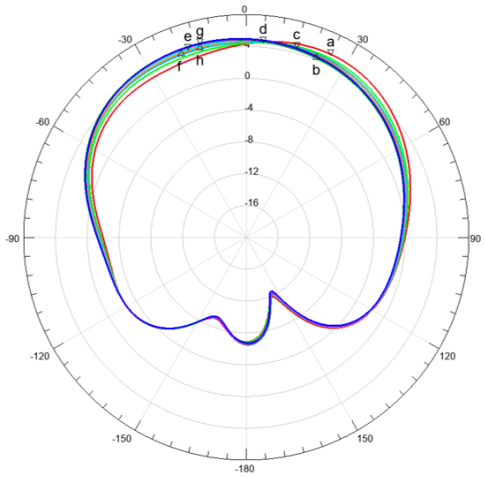

(a) Finely Vary C14, C25 = 1.76 pF; C36 = 3.2 pF, See Table 4.22, Scale 4

Fig. 4.17: Campaign B: Part 3, where C25 = 1.76 pF, C36 = 3.2 pF.

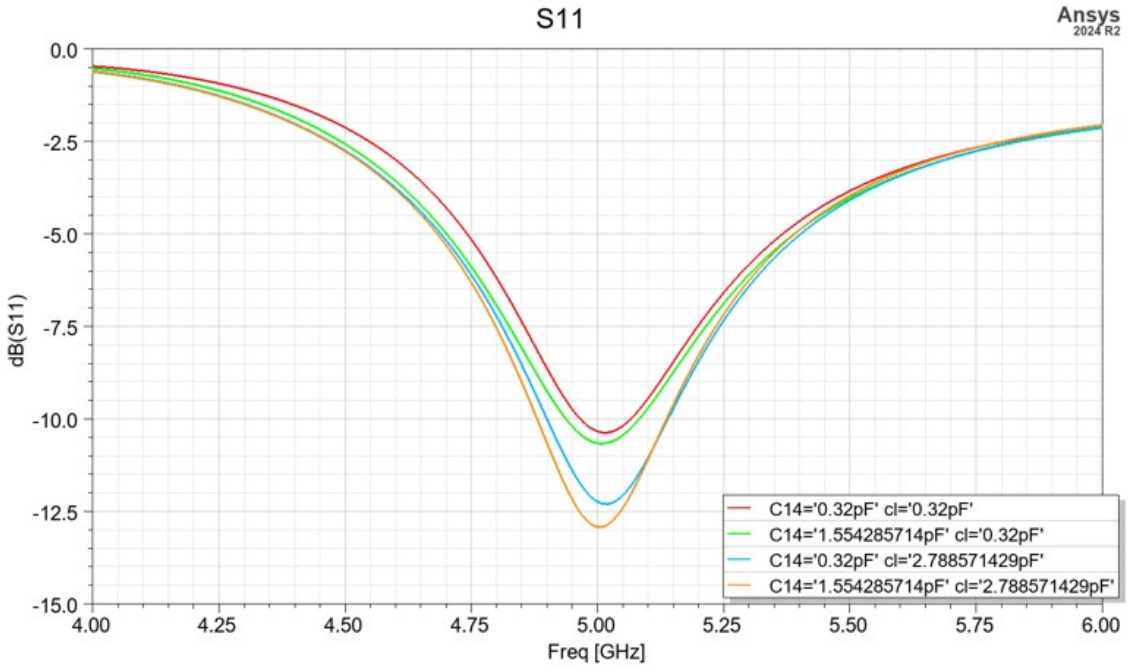

Fig. 4.18: Selected S11 Plots of Campaign B

Table 4.9: Coarsely Vary C14, C25 = C36 = 0.32 pF, Scale 1, Fig. 4.14a

C14 (pF)	C25 (pF)	C36 (pF)	Realized Gain (dB)	Beamsteering Angle (°)
0.32	0.32	0.32	3.9	23.9
0.73	0.32	0.32	5.1	−28.8
1.14	0.32	0.32	5.4	−27.1
1.55	0.32	0.32	5.5	−28.1
1.97	0.32	0.32	5.6	−27.7
2.38	0.32	0.32	5.8	−28.4
2.79	0.32	0.32	5.7	−28.4
3.2	0.32	0.32	5.8	−28.7

Table 4.10: Finely Vary C14, C25 = C36 = 0.32 pF, Scale 5, Fig. 4.14b

C14 (pF)	C25 (pF)	C36 (pF)	Realized Gain (dB)	Beamsteering Angle (°)
0.32	0.32	0.32	3.9	24.0
0.38	0.32	0.32	4.4	−27.5
0.41	0.32	0.32	4.6	−28.0
0.51	0.32	0.32	4.6	−27.9
0.61	0.32	0.32	4.8	−27.6
0.67	0.32	0.32	5.1	−28.4
0.73	0.32	0.32	5.1	−28.8
0.8	0.32	0.32	5.3	−29.0

Table 4.11: Coarsely Vary C14, C25 = C36 = 0.73 pF, Scale 1, Fig. 4.14c

C14 (pF)	C25 (pF)	C36 (pF)	Realized Gain (dB)	Beamsteering Angle (°)
0.32	0.73	0.73	5.0	22.8
0.73	0.73	0.73	4.8	−1.7
1.14	0.73	0.73	4.8	−9.7
1.55	0.73	0.73	4.8	−10.5
1.97	0.73	0.73	4.8	−10.2
2.38	0.73	0.73	4.8	−9.2
2.79	0.73	0.73	4.8	−5.3
3.2	0.73	0.73	4.8	−3.0

Table 4.12: Finely Vary C14, C25 = C36 = 0.73 pF, Scale 1, Fig. 4.14d

C14 (pF)	C25 (pF)	C36 (pF)	Realized Gain (dB)	Beamsteering Angle (°)
0.32	0.73	0.73	5.0	22.8
0.73	0.73	0.73	4.9	20.5
1.14	0.73	0.73	4.7	15.5
1.55	0.73	0.73	4.7	11.8
1.97	0.73	0.73	4.7	6.3
2.38	0.73	0.73	4.7	−2.5
2.79	0.73	0.73	4.8	−1.7
3.2	0.73	0.73	4.8	−4.3

Table 4.13: Coarsely Vary C14, C25 = C36 = 1.14 pF, Scale 1, Fig. 4.14e

C14 (pF)	C25 (pF)	C36 (pF)	Realized Gain (dB)	Beamsteering Angle (°)
0.32	1.14	1.14	5.3	24.7
0.73	1.14	1.14	4.8	5.56
1.14	1.14	1.14	5.0	−1.3
1.55	1.14	1.14	5.0	−0.2
1.97	1.14	1.14	5.0	−3.3
2.38	1.14	1.14	5.1	0.1
2.79	1.14	1.14	5.0	3.3
3.2	1.14	1.14	5.0	0.1

Table 4.14: Finely Vary C14, C25 = C36 = 1.14 pF, Scale 2, Fig. 4.14f

C14 (pF)	C25 (pF)	C36 (pF)	Realized Gain (dB)	Beamsteering Angle (°)
0.32	1.14	1.14	5.3	24.7
0.39	1.14	1.14	5.2	23.2
0.46	1.14	1.14	4.9	18.9
0.53	1.14	1.14	4.9	17.0
0.59	1.14	1.14	4.79	8.9
0.66	1.14	1.14	4.8	7.7
0.73	1.14	1.14	4.8	5.5
0.8	1.14	1.14	4.8	−2.8

Table 4.15: Coarsely Vary C14, C25 = C36 = 1.97 pF, Scale 1, Fig. 4.15a

C14 (pF)	C25 (pF)	C36 (pF)	Realized Gain (dB)	Beamsteering Angle (°)
0.32	1.97	1.97	5.3	21.8
0.73	1.97	1.97	4.9	−3.8
1.14	1.97	1.97	4.9	−4.2
1.55	1.97	1.97	5.1	−3.8
1.97	1.97	1.97	5.2	−2.2
2.38	1.97	1.97	5.1	−1.4
2.79	1.97	1.97	5.1	0.4
3.2	1.97	1.97	5.1	3.5

Table 4.16: Finely Vary C14, C25 = C36 = 1.96 pF, Scale 2, Fig. 4.15b

C14 (pF)	C25 (pF)	C36 (pF)	Realized Gain (dB)	Beamsteering Angle (°)
0.32	1.97	1.97	5.3	21.9
0.39	1.97	1.97	5.2	19.4
0.46	1.97	1.97	4.9	13.1
0.53	1.97	1.97	4.9	11.4
0.59	1.97	1.97	4.8	6.8
0.66	1.97	1.97	4.9	0.2
0.73	1.97	1.97	4.9	−4.2
0.8	1.97	1.97	5.0	−2.4

Table 4.17: Coarsely Vary C14, C25 = C36 = 3.2 pF, Scale 1, Fig. 4.15c

C14 (pF)	C25 (pF)	C36 (pF)	Realized Gain (dB)	Beamsteering Angle (°)
0.32	3.2	3.2	5.5	21.3
0.73	3.2	3.2	5.0	−3.5
1.14	3.2	3.2	5.1	−9.9
1.55	3.2	3.2	5.2	−9.1
1.97	3.2	3.2	5.2	−6.5
2.38	3.2	3.2	5.2	−3.6
2.79	3.2	3.2	5.2	−3.4
3.2	3.2	3.2	5.2	−3.3

Table 4.18: Finely Vary C14, C25 = C36 = 3.2 pF, Scale 2, Fig. 4.15d

C14 (pF)	C25 (pF)	C36 (pF)	Realized Gain (dB)	Beamsteering Angle (°)
0.32	3.2	3.2	5.5	21.3
0.39	3.2	3.2	5.1	18.6
0.46	3.2	3.2	5.0	13.4
0.53	3.2	3.2	4.9	7.4
0.59	3.2	3.2	4.9	3.8
0.66	3.2	3.2	5.0	−1.7
0.73	3.2	3.2	5.0	−3.5
0.8	3.2	3.2	5.1	−8.1

Table 4.19: Finely Vary C14, C25 = 1.0 pF, C36 = 0.32 pF, Scale 2, Fig. 4.16a

C14 (pF)	C25 (pF)	C36 (pF)	Realized Gain (dB)	Beamsteering Angle (°)
0.32	1.0	0.32	4.6	−4.5
0.39	1.0	0.32	4.62	−14.3
0.46	1.0	0.32	4.8	−17.8
0.53	1.0	0.32	4.9	−19.1
0.59	1.0	0.32	5.0	−21.3
0.66	1.0	0.32	5.0	−22.4
0.73	1.0	0.32	5.1	−23.1
0.8	1.0	0.32	5.3	−22.8

Table 4.20: Finely Vary C14, C25 = 1.0 pF, C36 = 2.0 pF, Scale 3, Fig. 4.16b

C14 (pF)	C25 (pF)	C36 (pF)	Realized Gain (dB)	Beamsteering Angle (°)
0.32	1.0	2.0	5.4	24.8
0.39	1.0	2.0	5.0	21.7
0.4	1.0	2.0	4.8	17.1
0.5	1.0	2.0	4.7	10.4
0.6	1.0	2.0	4.8	0.3
0.73	1.0	2.0	4.8	0
0.8	1.0	2.0	4.8	−4.2
0.9	1.0	2.0	4.9	−6.3
1.0	1.0	2.0	4.9	−6.8

Table 4.21: Finely Vary C14, C25 = 1.0 pF, C36 = 3.2 pF, Scale 3, Fig. 4.16c

C14 (pF)	C25 (pF)	C36 (pF)	Realized Gain (dB)	Beamsteering Angle (°)
0.32	1.0	3.2	5.3	25.0
0.39	1.0	3.2	5.0	23.1
0.4	1.0	3.2	4.9	21.9
0.5	1.0	3.2	4.7	16.3
0.6	1.0	3.2	4.6	5.1
0.73	1.0	3.2	4.8	−16.8
0.8	1.0	3.2	5.0	−19.1
0.9	1.0	3.2	5.0	−13.4
1.0	1.0	3.2	5.0	−13.3

Table 4.22: Finely Vary C14, C25 = 1.76 pF, C36 = 3.2 pF, Scale 1, Fig. 4.17a (Scale 4)

C14 (pF)	C25 (pF)	C36 (pF)	Realized Gain (dB)	Beamsteering Angle (°)
0.32	1.76	3.2	5.5	22.4
0.42	1.76	3.2	5.0	−4.5
0.51	1.76	3.2	5.2	−8.1
0.61	1.76	3.2	5.3	−6.4
0.71	1.76	3.2	5.3	−5.4
0.81	1.76	3.2	5.3	−4.8
0.90	1.76	3.2	5.3	−3.4

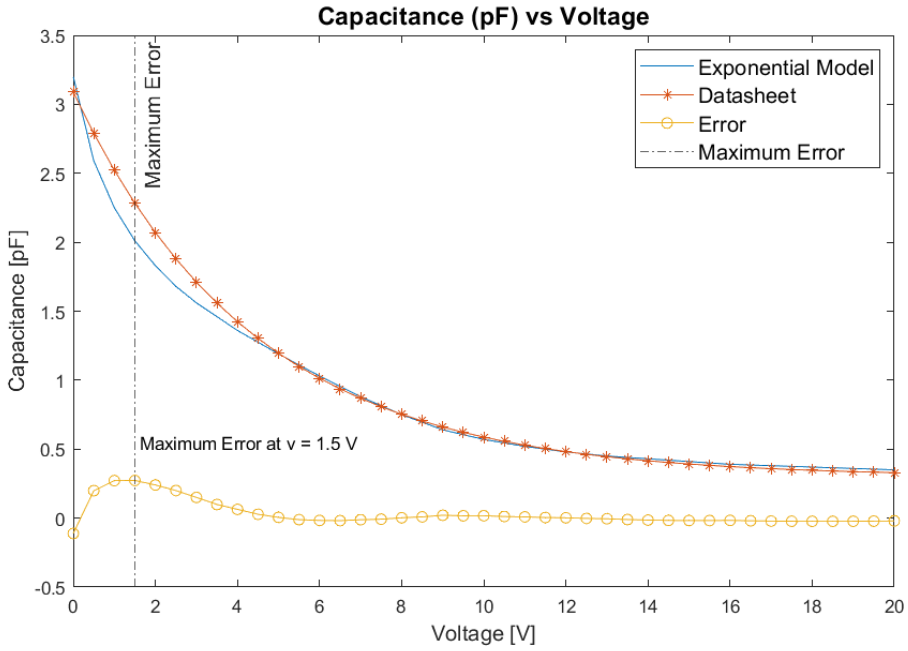

Fig. 4.19: Capacitance of Varactor vs. Applied Reverse Bias Voltage

4.4 Voltage-xz-Plane Beamsteering Relation

An equation to relate reverse bias voltage along the right varactor to xz-beamsteering angle was created. Varactors C1-C3 were set to 3.2 pF, while c4-c6 were swept. Based on the information in the varactor datasheet [39], the relationship between voltage and capacitance (CV curve) was found to roughly follow the equation

$$C_p = 3.5\,exp\,(-\frac{V+1}{4.4}) + 0.3 \tag{4.1}$$

where

C_p is the capacitance across the varactor in pF

V is the applied reverse bias voltage in V

The CV curves from the datasheet and the model are shown in Fig. 4.19. The largest error between the datasheet and the model roughly occurs where the change in voltage has the least effect on the antenna beamsteering angle. The capacitance values and beamsteering angles from HFSS simulations are plotted in Fig. 4.20. By combining Eqn. 4.1 and the

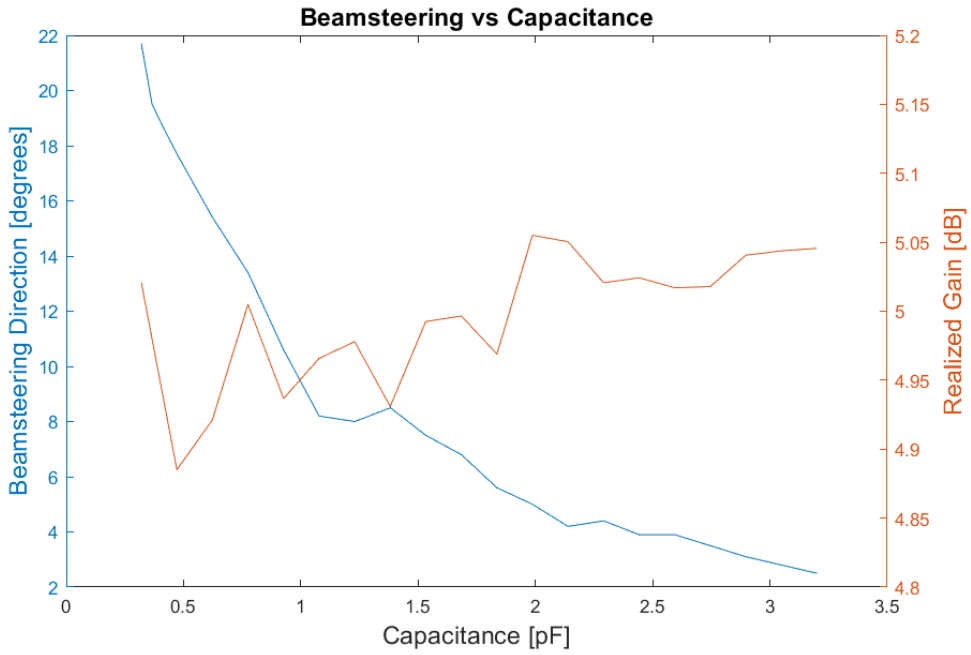

Fig. 4.20: Plot of Beamsteering Angle and Gain vs. Applied Reverse Bias Voltage applied to varactors on PPL RA

capacitance-beamsteering angle data shown in Fig. 4.20, the voltage-beamsteering angle curve was plotted. The voltage-antenna gain plot was also generated. See Fig. 4.21 for the relationship between voltage and beamsteering angle and antenna gain.

The gain varied by ∼2% over all voltages. The beamsteering angle varied from 23° to 2° over all voltages. Since only one side was varied and the antenna is symmetric across the xz-plane, the antenna as modeled is capable of beamsteering across the xz-plane from -23° to 23°. The direction control can be as fine as the voltage controller and manufacturing allows. Based on the simulations, the antenna is capable of fine beamsteering across both the xz- and yz-axes.

4.5 Varactor Planar Parasitic Layer Summary and Future Work

Varactors provide a feasible approach to achieve fine beamsteering on planar RAs. The antenna achieved fine beamsteering across $\theta \in \{-23, 23\}$; $\phi = 0$ and $\theta \in \{-25, 25\}$; $\phi = 90$. Further research efforts may include fabricating and measuring the antenna to verify the

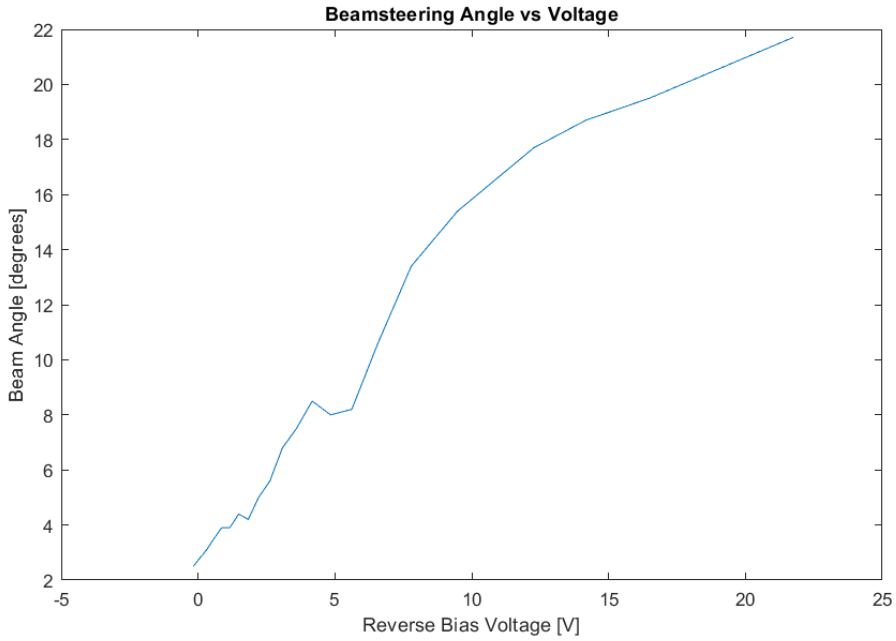

Fig. 4.21: Plot of Beamsteering Angle and Gain vs. Applied Reverse Bias Voltage applied to varactors on PPL RA

simulations. Other research may include beamsteering into other planes and wider ranges of varactor values, especially lower capacitance values. Further optimization of pixel sizes and shapes is another avenue for improvement. To practically implement the antenna, a lookup table for optimal settings for maximum gain into specific angles could be a useful product. Arrays of this type of RA will increase the gain and may improve beamsteering at low-elevation angles. A more comprehensive array could use different modes to reduce array sidelobes. A different geometry for the aperture may help to equalize the xz- and yz-planes, especially at boresight modes.

CHAPTER 5

Results and Model Construction of the Spherical Parasitic Layer (SPL) Reconfigurable Antenna (RA)

5.1 Spherical Parasitic Layer Antenna (SPL) Overview

The Spherical Parasitic Layer (SPL) reconfigurable antenna (RA) is a planar aperture-fed patch antenna resonant at 4.75 GHz with a spherical parasitic layer. In simulation, the SPL achieves wide-angle beamsteering up to 52 degrees in the xz-plane and realized gain up to 6.6 dB. See § 5.2 Table 5.7. The SPL was fabricated and its return loss was measured. See § 5.2.1.

5.1.1 SPL RA Construction

The Spherical Parasitic Layer (SPL) RA was based on previous work by Justin Wellington [2], whose model is shown in Fig. 5.1. This research extends his research by individually optimizing pixel length, gaps between pixels, patch antenna sizing, and bias line dimensions for maximum beam tilt and gain. The dimensions of the optimized antenna are shown in Table 5.1, Fig. 5.2, and Fig. 5.3.

The patch antenna is constructed on a PCB similarly to the PPL previously discussed. A polylactic acid (PLA) ($\epsilon_r = 2.1$) spherical dome created by 3D printing is overlaid the patch antenna. Copper pixels are overlaid the dome. Pixels consist of 0.5 oz copper with a rectangular cross-section projected along the z-axis onto the upper layer of the dome. This means that the actual length of the pixels varies with position on the dome. See Fig. 5.3, also Table 5.3, Appendix A.

The pixel length was optimized via parametric sweep to be 6.0 mm long. This length balances the need for low sidelobes at boresight (below 0 dB) and high gain at wide beam-steering angles and boresight. In consequence of the spherical nature of the dome, the

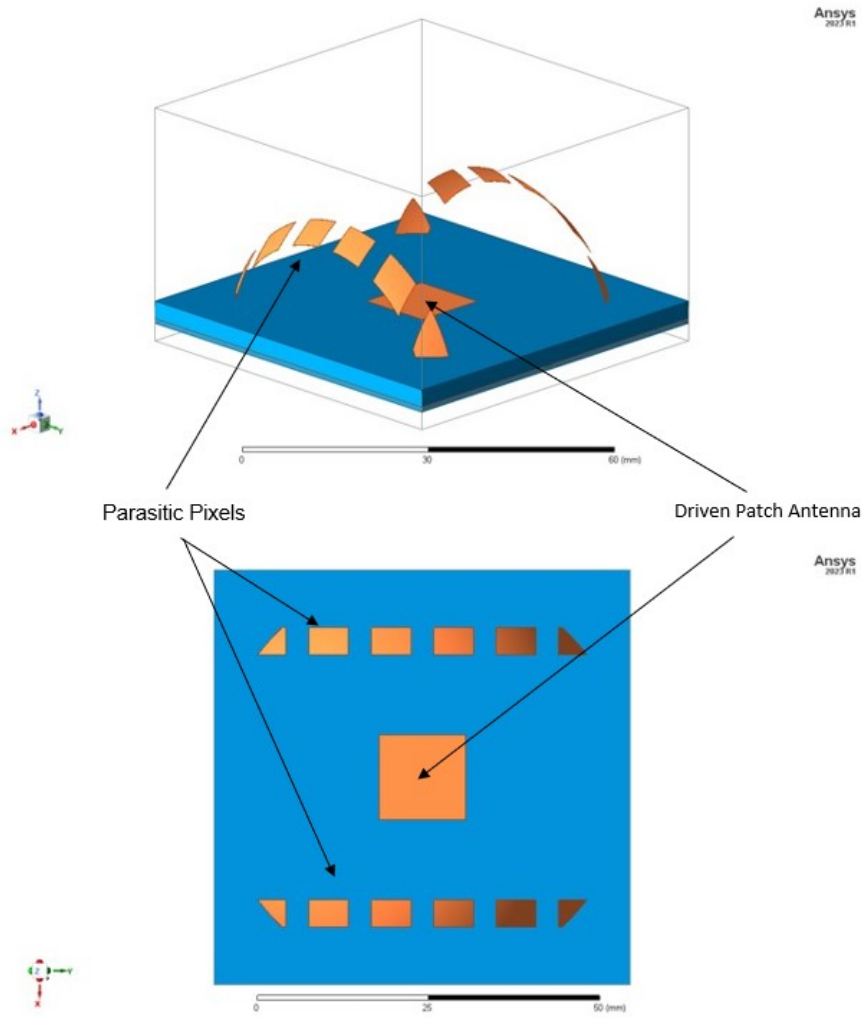

Fig. 5.1: Antenna simulated by Justin Wellington [2].

actual length of the pixels is longer than the planar length. The actual lengths are shown in Table 5.2 and were calculated using Eqn. A.3 derived in Appendix A. See also Fig. 5.4a. The overall lengths of connected pixels were also calculated and are shown in Figs. 5.4b, 5.4c.

PIN diodes were used to connect adjacent pixels. The PIN diodes were modeled as lumped RLC ports, with bias circuitry used in [1]. The diode schematic is shown in Fig. 5.5.

Table 5.1: Spherical Parasitic Layer Reconfigurable Antenna (SPL RA) Dimensions as seen in Fig. 5.2 and Fig. 5.3.

Dimension	Quantity (mm)
Substrate Length	61.0
Substrate Width	61.0
Substrate Height	3.0
Feedline Length	31.8
Feedline Width	1.8
Stub Length	2.8
Feed Height	0.8
Aperture Length	9.4
Aperture Width	0.8
Antenna Length	12.5
Antenna Width	12.7
Pixel Length	6.0
Pixel Width	4.0
Gap between Pixels	3.0
Pixel Offset	18.0
Bias Line Length	3.5
Bias Line Width	0.5
Choke Length	0.5
Bias Line Position Relative to Pixels	1.5
Dome Width	1.0
Internal Dome Radius	30.4
Dome Base Height	1.0
Copper Thickness	0.017

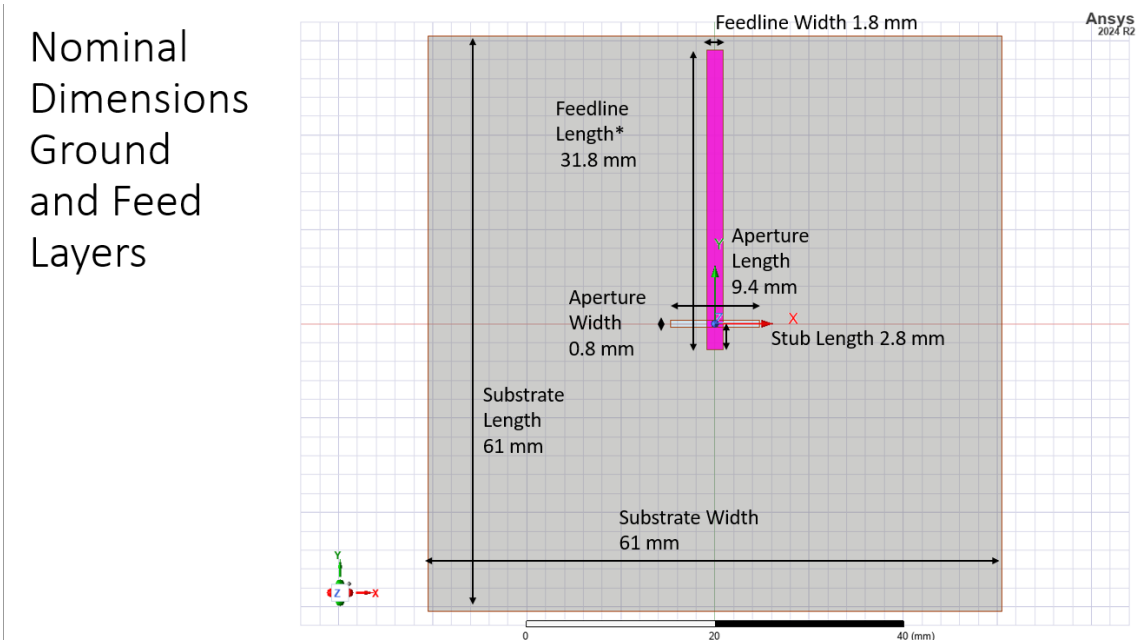

(a) Dome and Antenna Layers

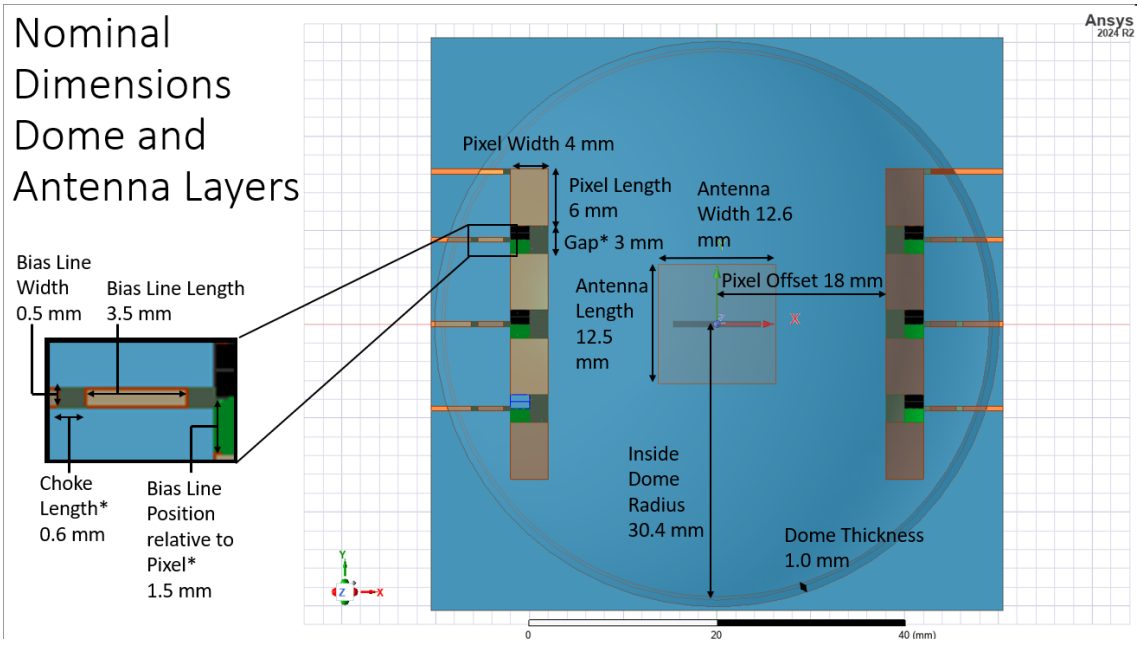

(b) Ground and Feed Layers

Fig. 5.2: Dome Antenna Dimensions

Table 5.2: SPL Pixel Dimensions, to be used with Fig. 5.4a.

Position Number	SP_x		SP_y	
-	Physical Length (mm)	Electrical Length (λ)	Physical Length (mm)	Electrical Length (λ)
1	5.3	0.12	6.1	0.14
2	5.2	0.12	6.1	0.14
3	6.1	0.14	7.1	0.16
4	5.5	0.13	7.6	0.17

Table 5.3: Combined SPL Pixel Dimensions, to be used with Figs. 5.4b, 5.4c. Derived by equations in Appendix A

Position Number	SP_x		SP_y	
-	Physical Length (mm)	Electrical Length (λ)	Physical Length (mm)	Electrical Length (λ)
Two Pixels Combined - 1	5.3	0.12	17.0	0.4
Two Pixels Combined - 2	5.5	0.13	16.4	0.4
Four Pixels Combined - 1	5.3	0.12	35.8	0.8
Four Pixels Combined - 2	5.5	0.13	37.1	0.9

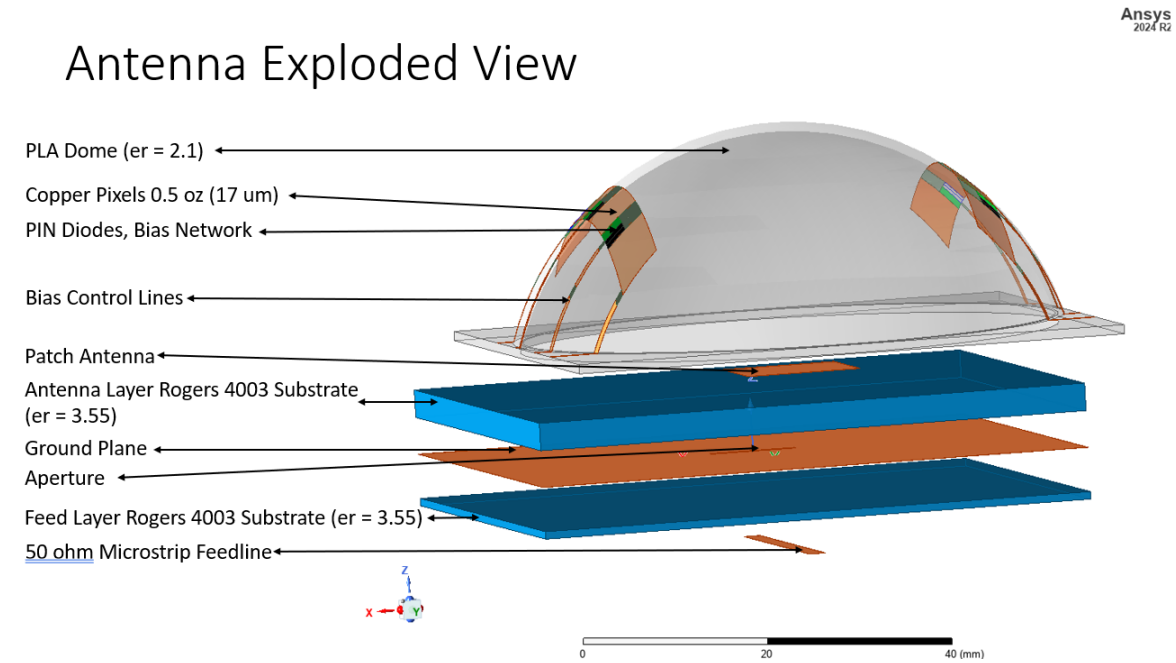

(a) SPL RA exploded view, skew view

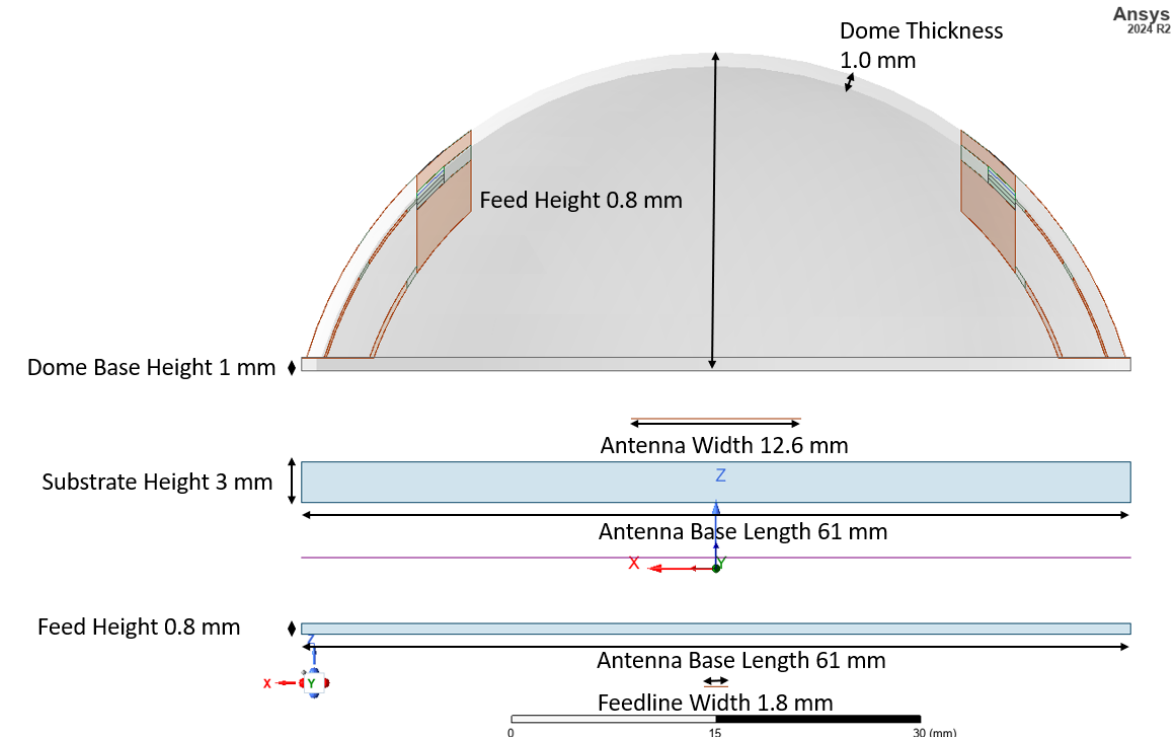

(b) SPL RA exploded view, $+x$-direction

Fig. 5.3: Exploded view of SPL RA, also see Table 5.1 and Fig. 5.2.

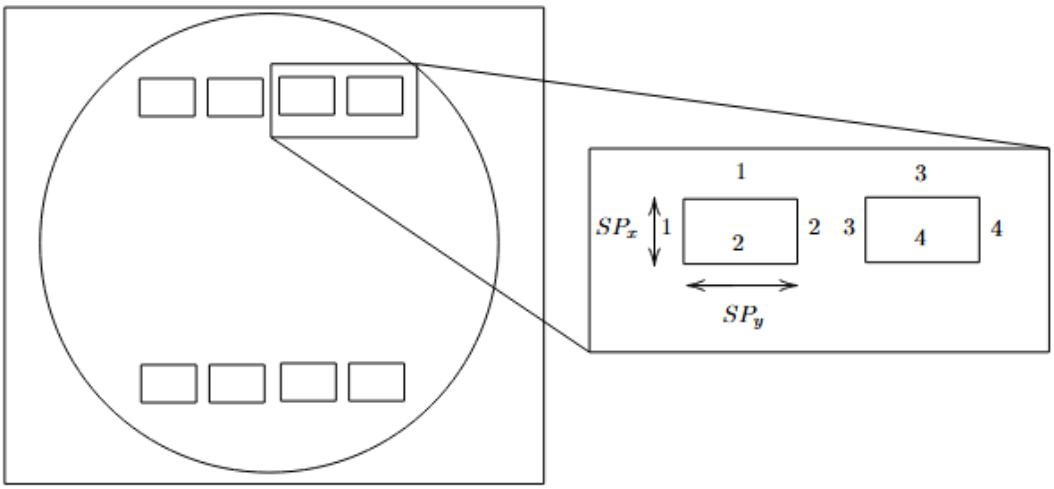

(a) Diagram to show individual pixel dimensions with Table 5.2.

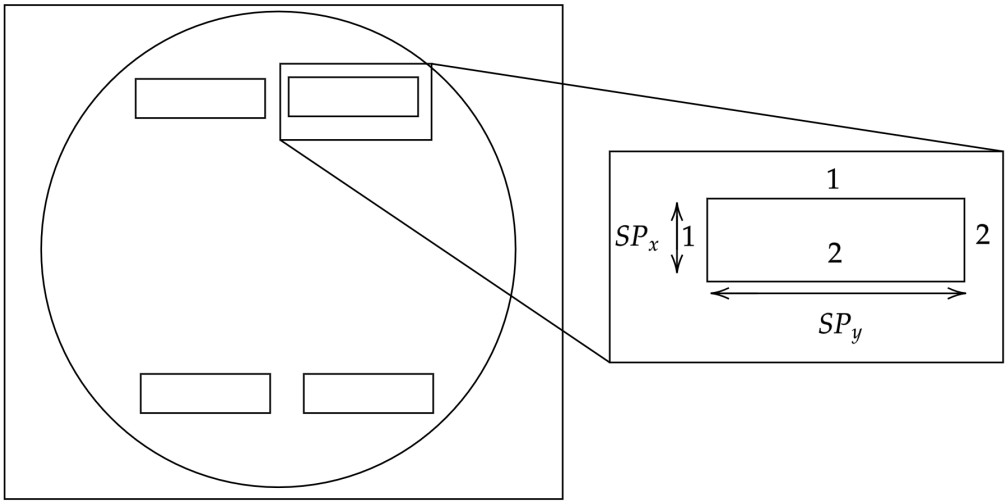

(b) Diagram to show dimensions of two connected pixels. See Table 5.3.

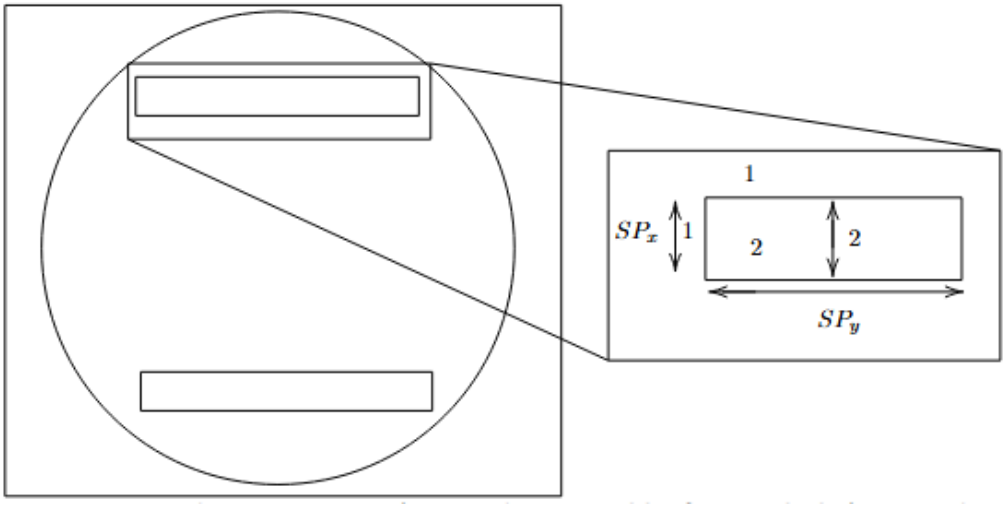

(c) Diagram to show dimensions of four connected pixels. See Table 5.3.

Fig. 5.4: Diagram of connected pixels for use with Tables 5.2, 5.3.

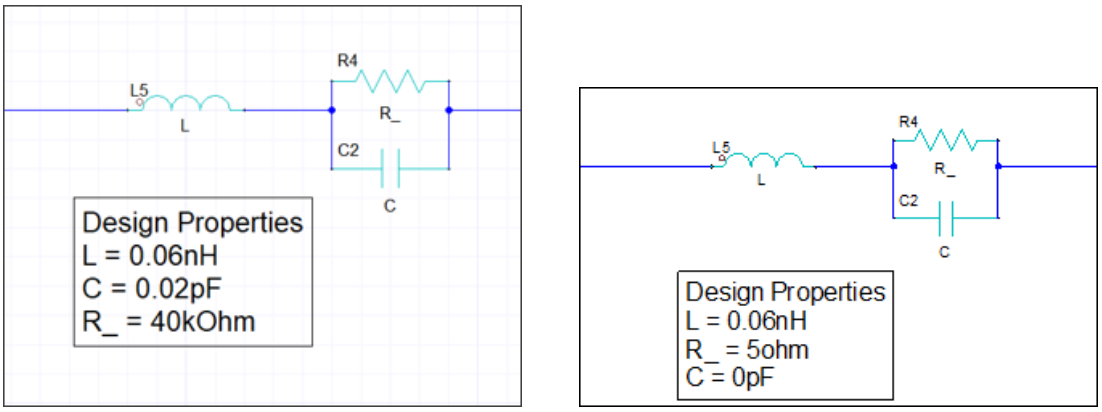

(a) PIN Diode OFF (b) PIN Diode ON

Fig. 5.5: PIN Diode Schematic

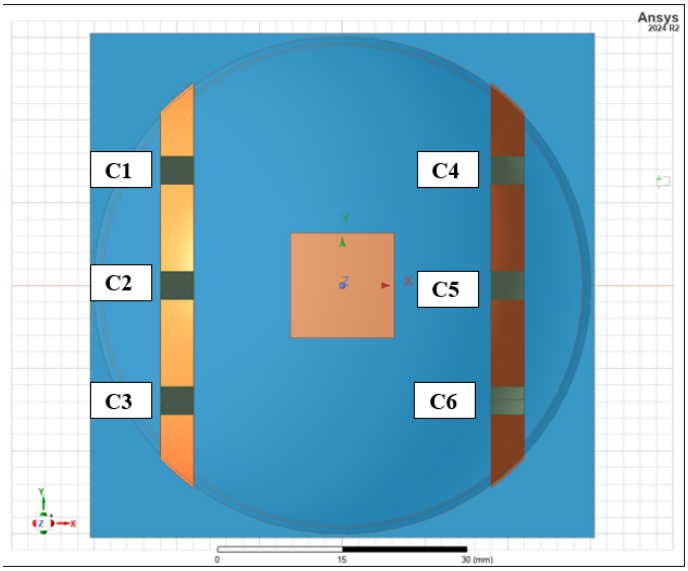

Fig. 5.6: PIN Diode numbering on SPL

Table 5.4: Spherical Parasitic Layer Reconfigurable Antenna (SPL RA) Modes

Mode Number	Mode Name	Mode Code	Max Gain (dB)	Beam Tilt ($\phi = 0°$)	Image
1	Left Extremes ON, Right OFF	101 000	5.78	47.3°	5.7
2	Left ON, Right OFF	111 000	6.59	35.5°	5.8
3	Boresight	000 000	5.16	-0.8°	5.9
4	Left OFF, Right ON	000 111	6.63	-34.9°	5.10
5	Left OFF, Right Extremes ON	000 101	5.46	-45.3°	5.11

5.1.2 SPL Modes

Five basic modes were simulated, shown in Table 5.4. The mode code shows which PIN diodes are ON. The digits refer to diodes c1-c6, as shown in Fig. 5.6. Each individual pixel measures 4 mm in the x-direction, and 6 mm in the y-direction. The actual dimensions (electrical and physical) are given in Table 5.2. The pixels may be connected through PIN diode switching to form an extended pixel as seen in Fig. 5.4b, 5.4c.

The PPL RA achieved a maximum angle of 24.8° with a gain of 5.4 dB. The SPL RA showed significant improvement in beamsteering angle, with a maximum angle of 47.3°. The gain improved to 5.8 dB.

Mode 3, where all the pixels are unconnected, creates a single main lobe at boresight. See Fig. 5.9. It was predicted that beamsteering would be greatest for modes 2 and 4, where the reflector length is the longest. However, the greatest gain occurred with modes 1 and 5, where the reflectors are closest to $\frac{\lambda}{2}$. See Figs. 5.7 - 5.11.

The return losses were also simulated. See Figs. 5.7 – 5.11 and compare with Fig. 5.14 in § 5.2.1.

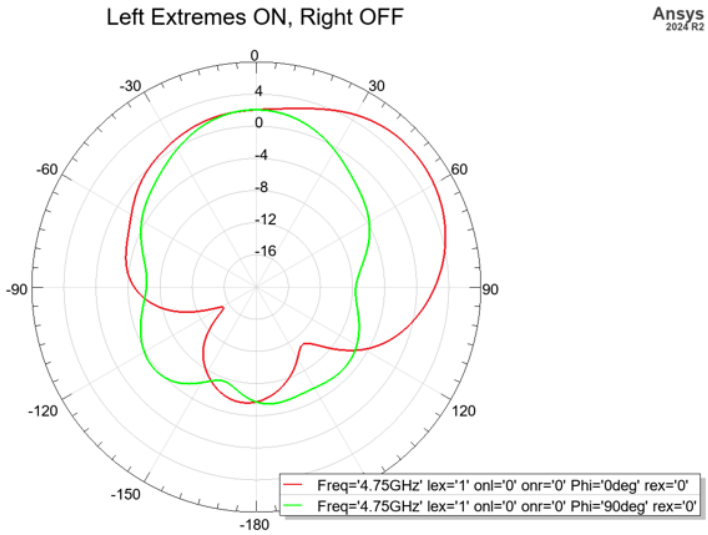

(a) Far-Field Radiation Plot, Original

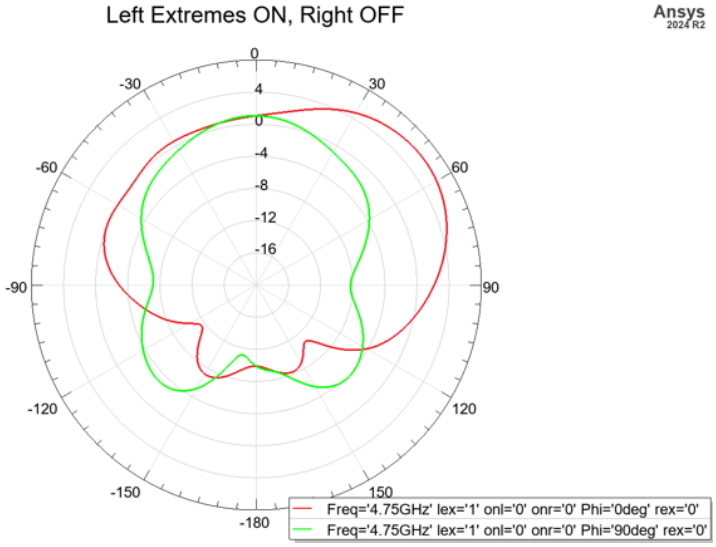

(b) Far-Field Radiation Plot, Fabricated

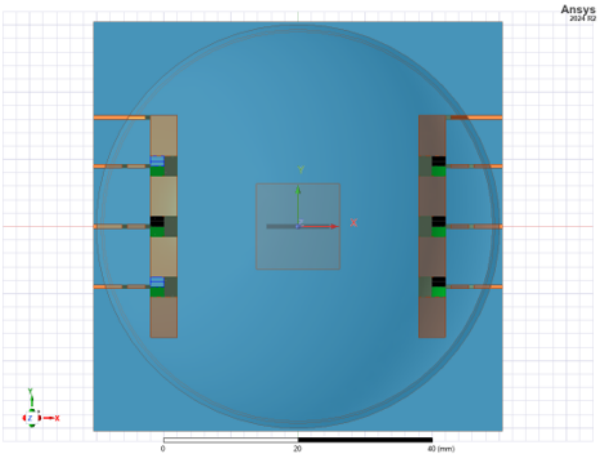

(c) Antenna Mode (Blue Indicates ON)

Fig. 5.7: Left Extremes ON, Right OFF Code: 101 000

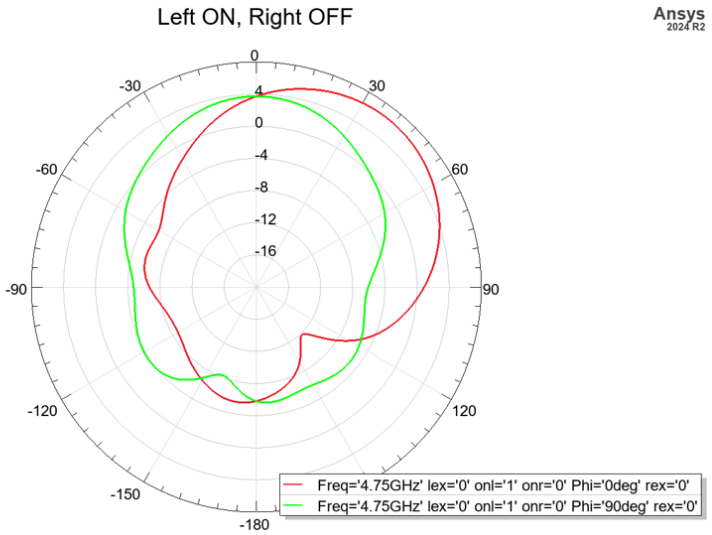

(a) Far-Field Radiation Plot, Original

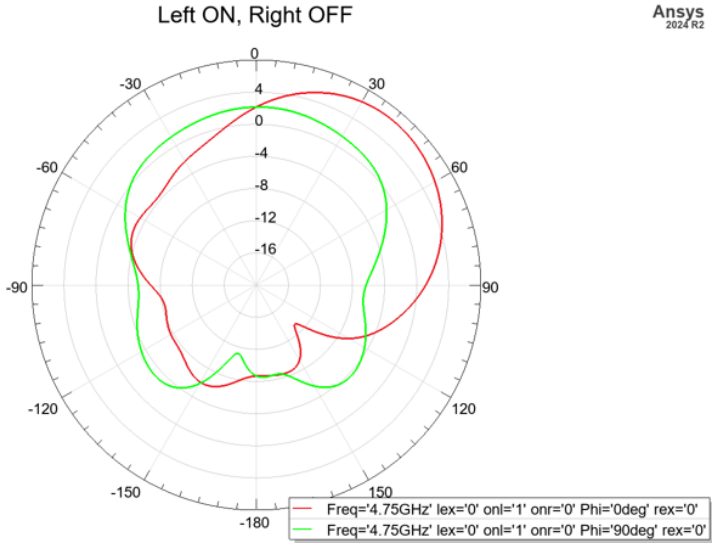

(b) Far-Field Radiation Plot, Fabricated

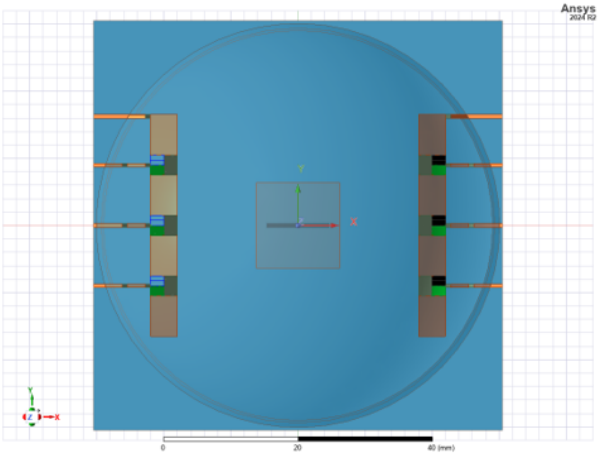

(c) Antenna (Blue Indicates ON)

Fig. 5.8: Left ON, Right OFF Code: 111 000

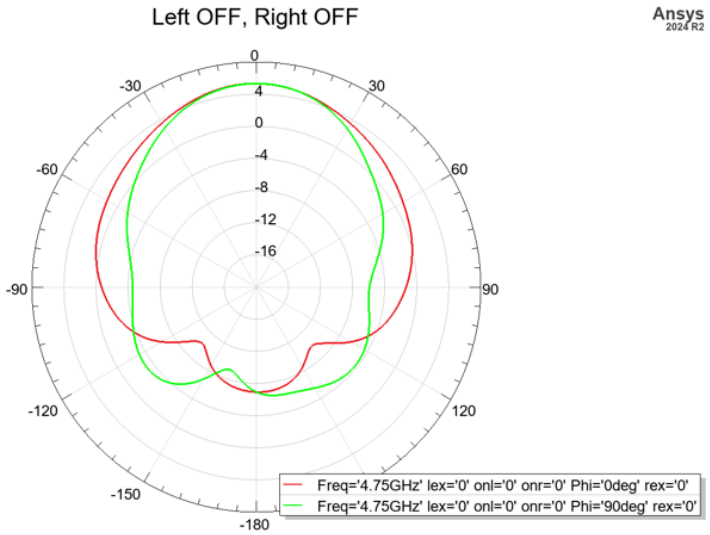

(a) Far-Field Radiation Plot, Original

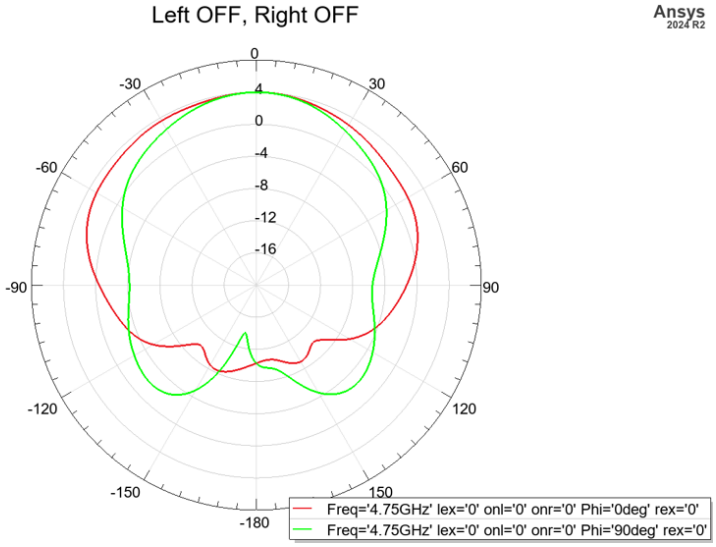

(b) Far-Field Radiation Plot, Fabricated

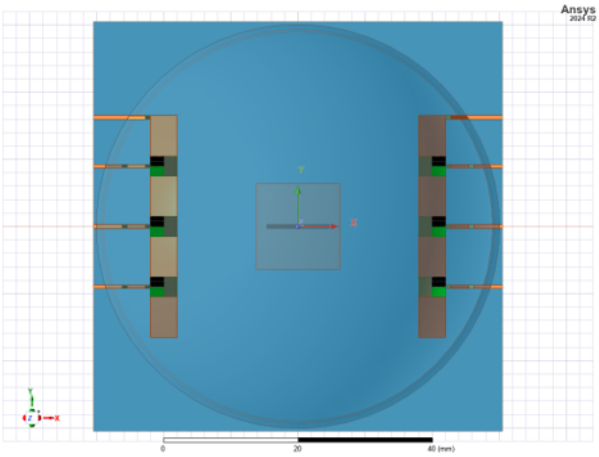

(c) Antenna (Blue Indicates ON)

Fig. 5.9: Boresight Code: 000 000

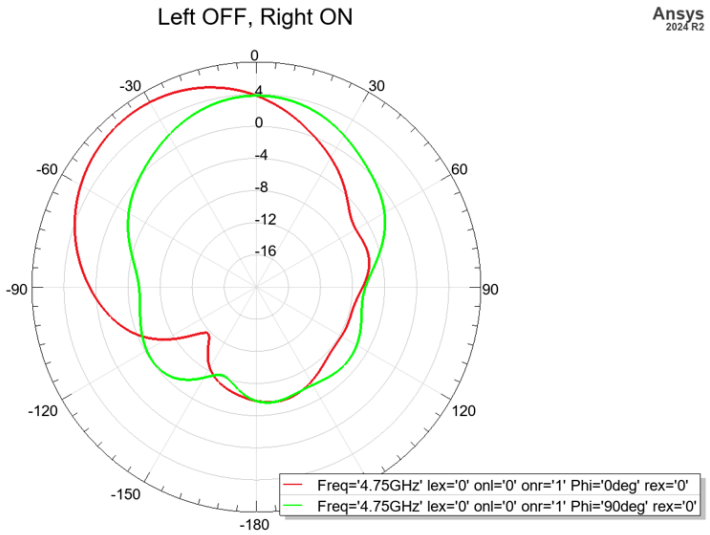

(a) Far-Field Radiation Plot, Original

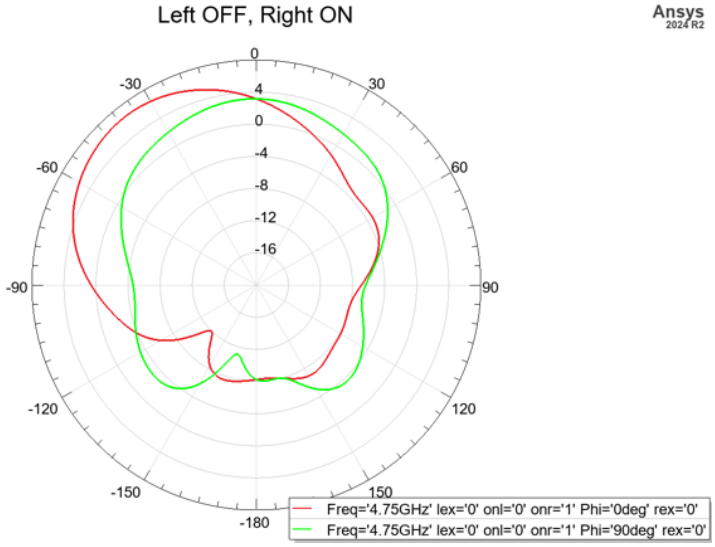

(b) Far-Field Radiation Plot, Fabricated

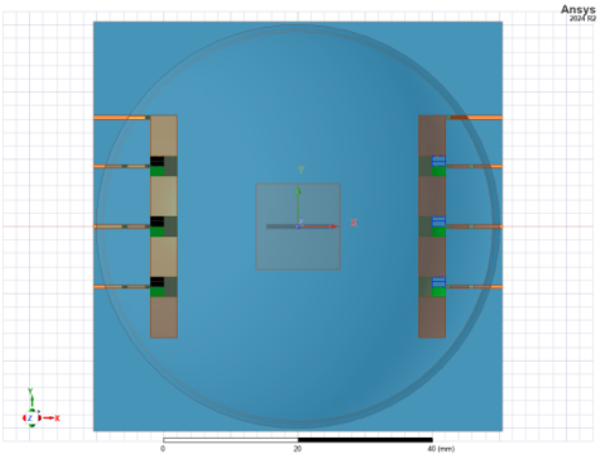

(c) Antenna (Blue Indicates ON)

Fig. 5.10: Left OFF, Right ON Code: 000 111

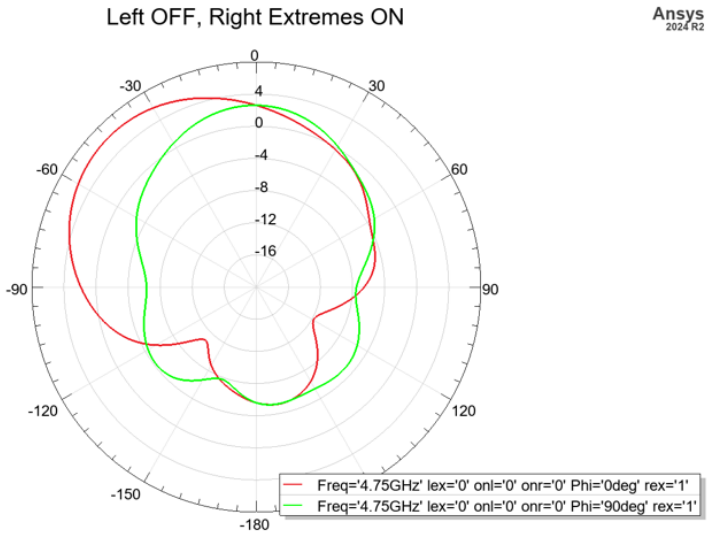

(a) Far-Field Radiation Plot, Original

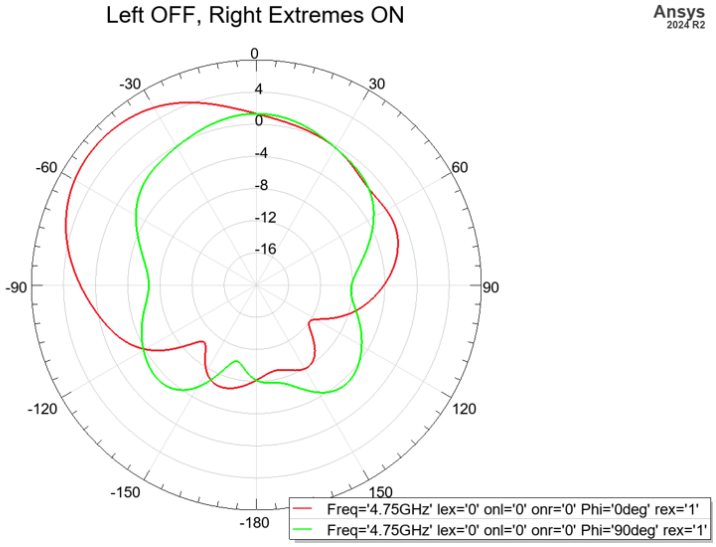

(b) Far-Field Radiation Plot, Fabricated

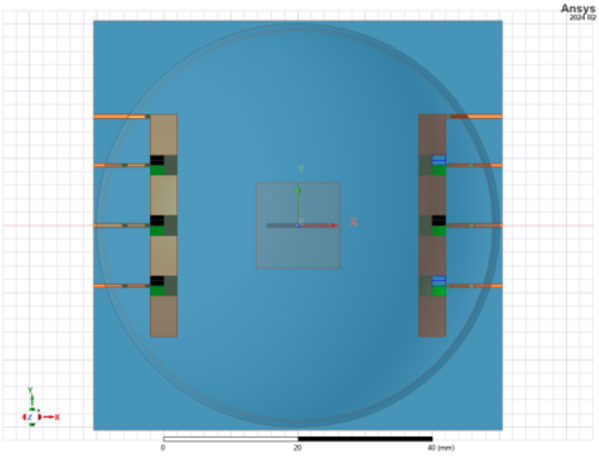

(c) Antenna (Blue Indicates ON)

Fig. 5.11: Left OFF, Right Extremes ON Code: 000 101

5.2 Spherical Parasitic Layer (SPL) Antenna Fabrication

The antenna model was modified to incorporate fabrication details. The dimensions, antenna, and results are shown in Tables 5.5, 5.6, and Fig. 5.12.

A Tachyon-100G pre-impregnated layer (prepreg) ($\epsilon_r = 3.06, \delta = 0.0017, 2$ mils), was added between various layers of Rogers 4003 ($\epsilon_r = 3.38, \delta = 0.0021$) to form a substrate. The stackup is shown in Table 5.6. The stackup was introduced in the HFSS model and parametric sweeps were run on the substrate thickness. The substrate thickness above the ground plane (aperture thickness) has little effect on the antenna at resonance. [18] suggests the primary result is a loss of bandwidth. The prepreg layers introduced 0.3 dB of loss. The mounting holes were filled with a stainless steel conductive cylinder and a nylon ($\epsilon_r = 3$) cylinder, modeling a screw or pin respectively to hold the dome in place. The cylinder diameter was set as 2.4 mm. The maximum gain and sidelobe gain at low angles were increased with the use of a conductive screw. A change in copper thickness to 1 oz was discovered to have little effect on the overall radiation performance. The dome width was varied. It was discovered that a thicker dome (2 mm) resulted in 0.1 dB/mm loss.

The overall result of adding the fabrication details was an increased gain at high beamsteering angles and a greater beamsteering capability. However, the boresight gain decreased by 1.2 dB. The results are compared in Table 5.7 and Figs. 5.7- 5.11.

5.2.1 Fabrication

The antenna PCB was fabricated using standard PCB fabrication techniques. The antenna dome was modeled in SolidWorks, a 3D modeling application. Indentations (0.5 mm deep) were added to the dome to facilitate tape attachment. The dome was printed using PLA filament. The dome was connected to the antenna PCB using 2 mm nylon screws. A Sub-Miniature version A (SMA) connector was hand-soldered to the feedline. 1 oz copper tape, measuring 0.25 in wide, was used to create pixels in two idealized configurations. The first (Type 1) is the equivalent of Mode 3, where each pixel is disconnected. The second (Type 2) is the equivalent of Mode 1, where the right pixels are disconnected and the left pixels are connected into two strips. The final antennas are shown in Fig. 5.13.

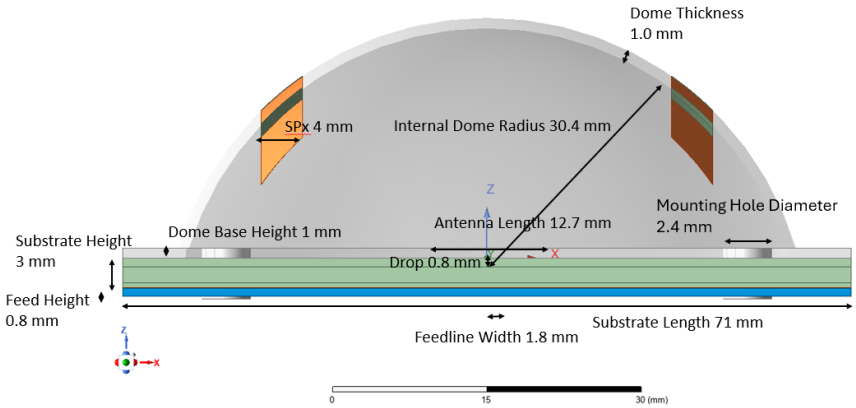

(a) Fabricated Antenna Dimensions from $-y$-direction

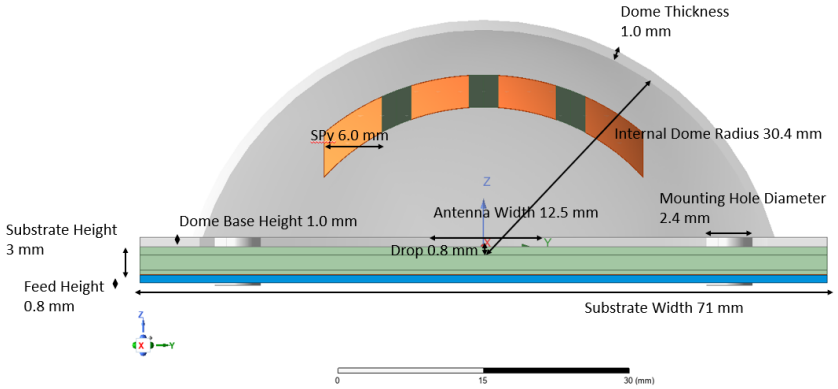

(b) Fabricated Antenna Dimensions from $+x$-direction

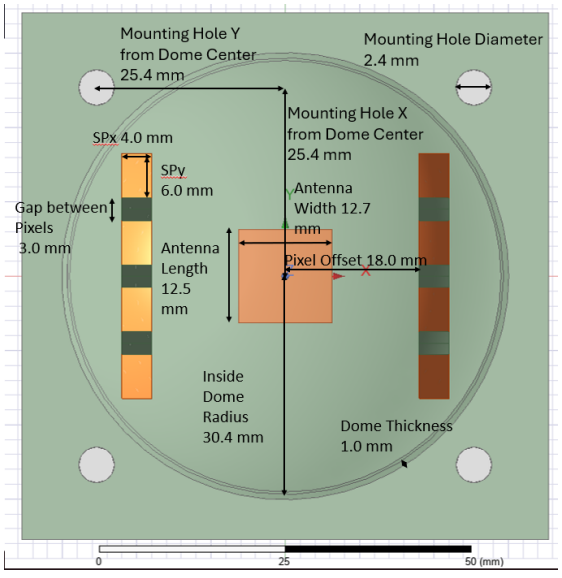

(c) Fabricated Antenna Dimensions from $+z$-direction

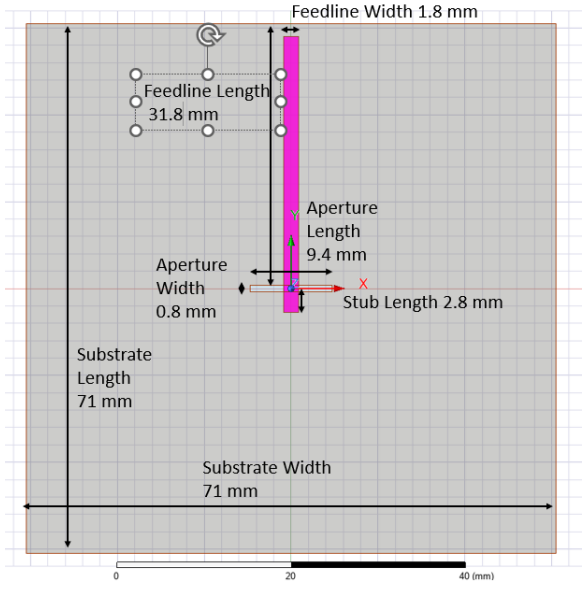

(d) Fabricated Antenna Dimensions from $-z$-direction

Fig. 5.12: Fabricated Antenna Dimensions

Table 5.5: Spherical Parasitic Layer Reconfigurable Antenna (SPL RA) fabrication dimensions as seen in Fig. 5.12. The stackup is given in Table 5.6.

Dimension	Quantity (mm)
Substrate Length	71.0
Substrate Width	71.0
Substrate Height	2.9
Feedline Length	31.8
Feedline Width	1.8
Stub Length	2.8
Feed Height	0.8
Aperture Length	9.4
Aperture Width	0.8
Antenna Length	12.5
Antenna Width	12.7
Pixel Length	6.0
Pixel Width	4.0
Gap between Pixels	3.0
Pixel Offset	18.0
Dome Width	0.5
Internal Dome Radius	30.4
Dome Base Height	1.0
Copper Thickness	0.017
Mounting Hole Diameter	2.4
Mounting Hole X, Y from dome center	25.4

Table 5.6: Spherical Parasitic Layer (SPL) Base Stackup

Purpose	Material Type	Dielectric Constant	Loss Tangent	Thickness
Patch	Copper	-	-	0.5 oz
Substrate	Rogers 4003	3.38	0.0021	0.81 mm
Prepreg	Tachyon-100G	3.06	0.0017	0.05 mm
Substrate	Rogers 4003	3.38	0.0021	1.52 mm
Prepreg	Tachyon-100G	3.06	0.0017	0.05 mm
Substrate	Rogers 4003	3.38	0.0021	0.41 mm
Prepreg	Tachyon-100G	3.06	0.0017	0.05 mm
Ground Plane	Copper	-	-	0.5 oz
Substrate	Rogers 4003	3.38	0.0021	0.81 mm
Feedline	Copper	-	-	0.5 oz

Mode Number	Mode	Original Beam-steering Angle	Original Gain	New Beam-steering Angle	New Gain	Plots
1	Left Extremes ON, Right OFF	5.78	47.3°	52.7	6.06	5.7
2	Left ON, Right OFF	6.59	35.5°	40.2°	6.62	5.8
3	Boresight	5.16	-0.8°	0.3°	3.98	5.9
4	Left OFF, Right ON	6.63	-34.9°	-38.3°	6.57	5.10
5	Left OFF, Right Extremes ON	5.46	-45.3°	-49.0°	6.43	5.11

Table 5.7: Comparison Table between original SPL and simulated fabricated SPL

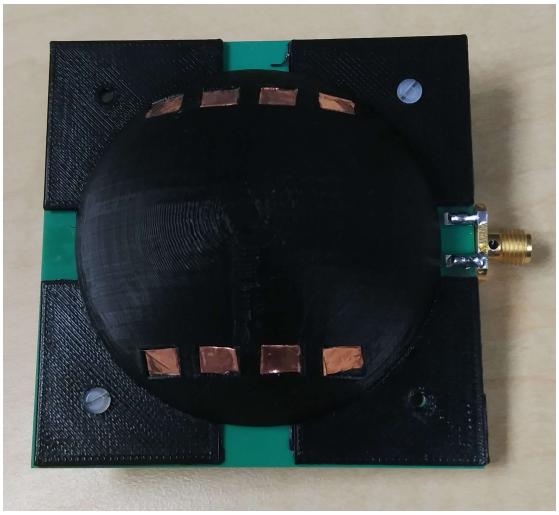

(a) Fabricated Antenna - Disconnected Pixels, Type 1

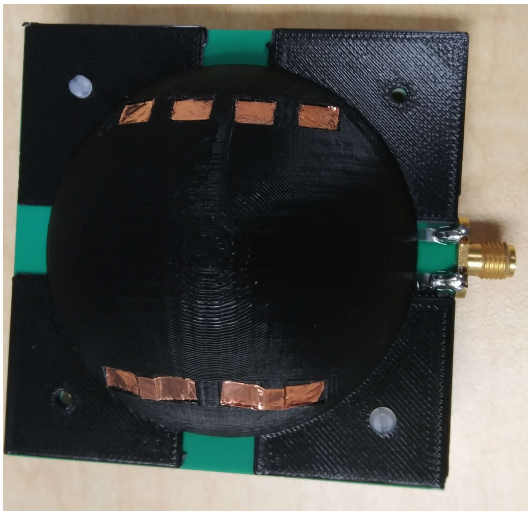

(b) Fabricated Antenna - Connected Pixels, Type 2

(c) Fabricated Antenna - Feedline Layer

Fig. 5.13: Fabricated Antennas used to measure S11

The return loss of the antenna was measured using a calibrated Anritsu 4647B VNA. The results are shown and compared against the simulated results in Fig. 5.14 and the results of each antenna base are compared in Fig. 5.15.

The results do not show a strong relationship between the simulated and the measured results. The fabricated Type 1 antenna (the base alone) shows a minimum S11 at 5.47 GHz and has a -10 dB bandwidth from 5.20 GHz to 5.65 GHz (0.25 GHz wide). The simulated Type 1 antenna shows a minimum S11 at 4.8 GHz and a -10 dB bandwidth from 4.65 to 4.95 GHz (0.3 GHz wide). The fabricated S11 plot shows two minima - one at 4.45 GHz at -7.5 dB and the other at 5.48 GHz at -15.5 dB. The simulated S11 plot has a single minimum at 4.8 GHz, less than -20 dB. The fabricated antenna Type 2 has a minimum S11 at 4.35 GHz and has a -10 dB bandwidth from 4.30 to 4.80 GHz (11%) once the dome is added. The 11% bandwidth is much larger than typical patch antenna ($\sim$3%) [19]. This likely arises from the aperture feed and the parasitic layers. The layers increase bandwidth as explained in [20]. The wide variation in the fabricated antennas indicates the design requires care in fabrication and connection to be consistent. It is expected that the differences between the antennas are due to variation in the soldered connections between the antenna and the SMA connection.

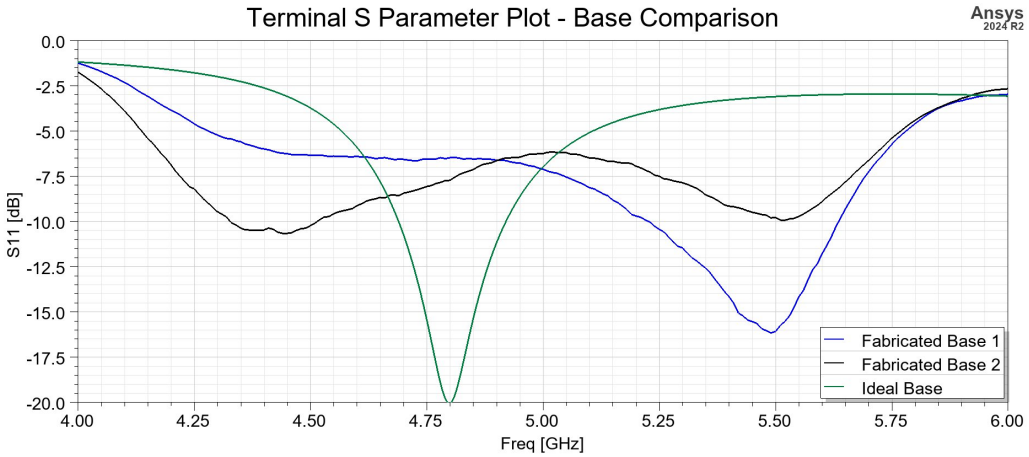

(a) S11 of bases without any spherical parasitic layer. Two bases (1, 2) were fabricated and measured. Despite being made from the same material and process, the bases are not identical.

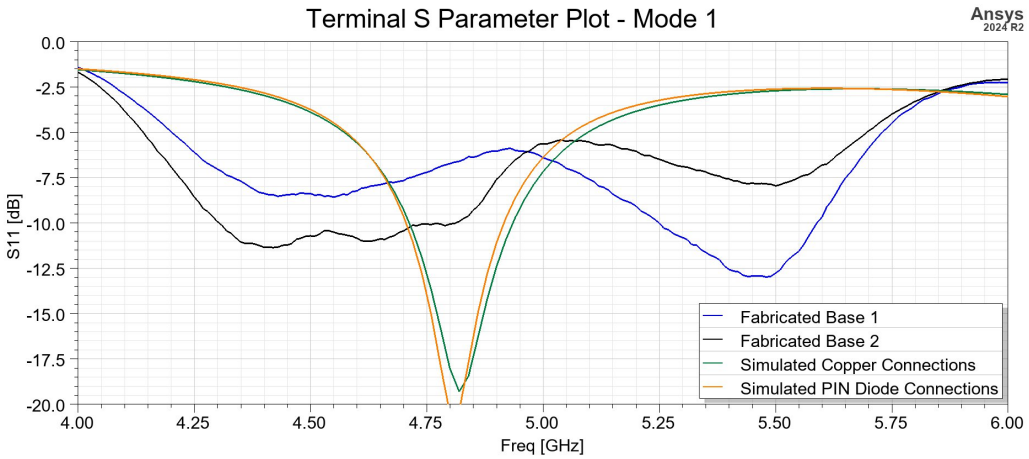

(b) Antenna Dome S11 - Mode 1

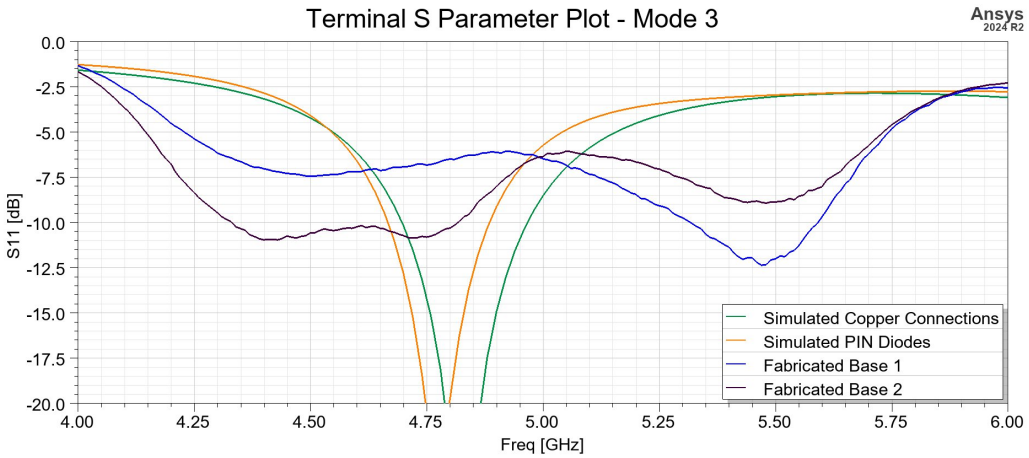

(c) Antenna Dome S11 - Mode 3, Boresight

Fig. 5.14: S11 Plots of both simulated and fabricated antennas

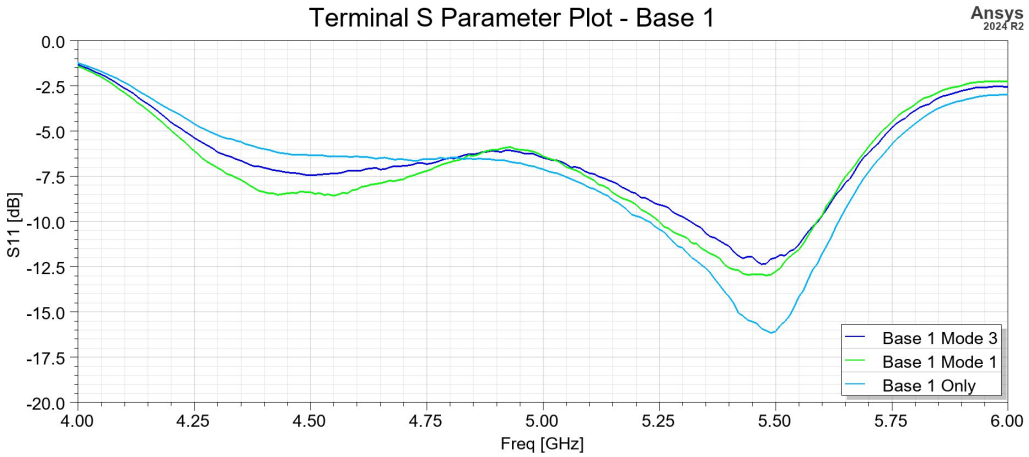

(a) Base 1 S11 Comparison

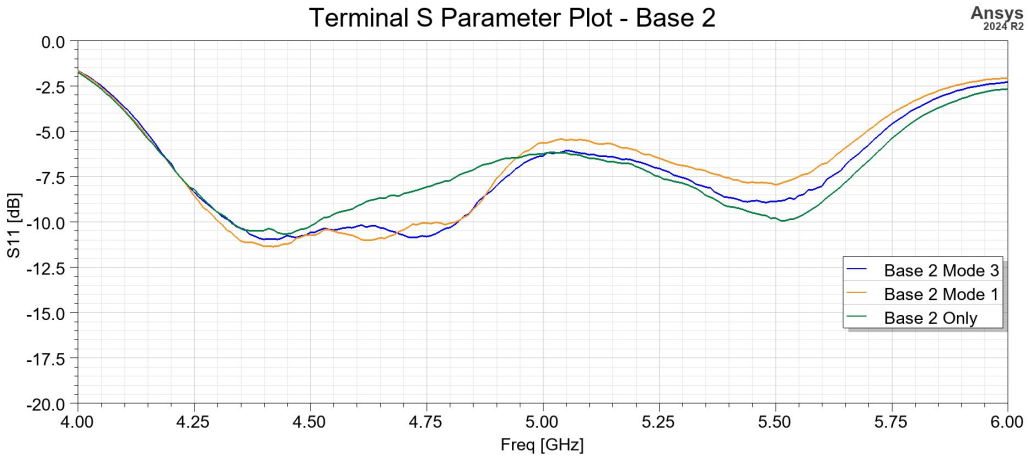

(b) Base 2 S11 Comparison

Fig. 5.15: Base S11 Comparison for all fabricated modes

5.3 Future Work

Future work includes measuring the radiation patterns of the antenna, and comparing simulated results to the measurements. Radiation testing for antennas is typically done using an anechoic chamber or near-field probes. USU has worked with the Technical University of Catalonia—Barcelona Tech (UPC), Barcelona, Spain, which has the largest academic anechoic chamber in Europe. It may be possible to partner with them to test the antenna. USU also owns an RF anechoic chamber that may be used.

The geometry of the antenna, such as the dome shape, may be changed to better steer in other ϕ-planes. The arrangement of pixels in a radial pattern may be useful in this regard. The dome may be changed to a different curve, such as a parabola, to improve gain. Another way to improve gain may be to make the pixels equally sized, adding a parasitic layer, adding a row of pixels, or a parasitic reflective surface.

The use of variable coupling (either varactor diodes or variable resistors) may allow for continuous beamsteering on the SPL. A combination of PIN diodes and variable elements could provide more degrees of freedom. A multi-frequency, beamsteering RA may be possible by implementing varactors on the patch, similar to [14, 26]. Bandwidth of the patch may be increased by adding a second layer, as shown in [20]. Arrays of this type of RA will increase the gain and may improve beamsteering at low-elevation angles.

Interest in this type of RA has been expressed by the USU unmanned aerial vehicles (UAVs) program. The program uses a frequency of 5.8 GHz to communicate from ground stations to UAVs. A future project could use a pair of similar antennas designed for 5.8 GHz to demonstrate this application. Practically, the GPS data from the UAV and ground station could provide an appropriate beamsteering vector. The vector could be input to a microcontroller or FPGA, and a lookup table with the appropriate mode could be consulted to achieve an optimal link budget.

CHAPTER 6

Conclusion

RAs provide an additional method to achieve antenna beamsteering in addition to phased-array and mechanically steered antennas. RAs can achieve large beamsteering angles and can eliminate power-hungry phase shifters and mechanical elements, resulting in improved weight and reliability. Overall, RAs can allow for antennas with lower SWaP, cost, and open opportunities for higher bandwidth systems and more efficient usage of the RF spectrum. The research demonstrates beamsteering using a two antenna variants. The first is a planar parasitic layer antenna uses varactors at 5 GHz to achieve beamsteering. The antenna achieved fine beamsteering from $\theta \in \{\pm 23^\circ, \pm 25^\circ\}; \phi \in \{0^\circ, 90^\circ\}$. The second is a spherical dome parasitic layer using PIN diodes to achieve beam steering. The antenna achieved beamsteering from $\theta \in \{-49^\circ, 52.7^\circ\}; \phi = 0^\circ$. The spherical parasitic layer antenna was fabricated and the return loss was measured. The antennas achieved a much larger bandwidth than the simulations, but at unexpected frequencies and differed across fabricated antennas. Future work includes measuring the radiation patterns. Potential future research includes implementing fine beam steering on the dome antenna, improving steering in the yz-plane, building an array of the antennas, improving bandwidth and tunability, and implementing a 5.8 GHz antenna as part of a drone communication system.

REFERENCES

[1] M. A. Towfiq, I. Bahceci, S. Blanch, J. Romeu, L. Jofre, and B. A. Cetiner, "A reconfigurable antenna with beam steering and beamwidth variability for wireless communications," *IEEE Transactions on Antennas and Propagation*, vol. 66, no. 10, pp. 5052–5063, 2018.

[2] J. Wellington, "Usu updated reconfigurable dome fabrication files," Feb. 2025, Private Communication.

[3] Weisstein, Eric W. (2025) Spherical coordinates. [Online]. Available: https://mathworld.wolfram.com/SphericalCoordinates.html

[4] B. Cetiner, "The fundamentals of mras," Nov. 2025, Private Communication.

[5] Y. Tawk, J. Costantine, and C. G. Christodoulou, "A varactor-based reconfigurable filtenna," *IEEE Antennas and Wireless Propagation Letters*, vol. 11, pp. 716–719, 2012.

[6] J. Costantine, Y. Tawk, S. E. Barbin, and C. G. Christodoulou, "Reconfigurable antennas: Design and applications," *Proceedings of the IEEE*, vol. 103, no. 3, pp. 424–437, 2015.

[7] A. Zandamela, N. Marchetti, M. J. Ammann, and A. Narbudowicz, "3-d beam-steering mimo antenna for on-body iot applications," *IEEE Transactions on Antennas and Propagation*, vol. 72, no. 3, pp. 2241–2251, 2024.

[8] D. Rodrigo, Y. Damgaci, M. Unlu, B. Cetiner, J. Romeu, and L. Jofre, "Antenna reconfigurability based on a novel parasitic pixel layer," in *Proceedings of the 5th European Conference on Antennas and Propagation (EUCAP)*, 2011, pp. 3497–3500.

[9] L. Pringle, P. Harms, S. Blalock, G. Kiesel, E. Kuster, P. Friederich, R. Prado, J. Morris, and G. Smith, "A reconfigurable aperture antenna based on switched links between electrically small metallic patches," *IEEE Transactions on Antennas and Propagation*, vol. 52, no. 6, pp. 1434–1445, 2004.

[10] J. T. Bernhard, *Antenna Engineering Handbook*. McGraw Hill, 2007, ch. 31 Reconfigurable Antennas, pp. 31–1–31–19.

[11] L.-M. Zhang, X. Ding, and B.-Z. Wang, "A low-cost beam steering antenna for indoor wireless communication," *IEEE Transactions on Antennas and Propagation*, vol. 70, no. 9, pp. 8548–8553, 2022.

[12] Y. Jin, F. Yang, S. Xu, and M. Li, "A fet-based reconfigurable reflectarray antenna with low power consumption," in *2022 International Conference on Microwave and Millimeter Wave Technology (ICMMT)*, 2022, pp. 1–3.

[13] G. D. King, M. A. Towfiq, and B. A. Cetiner, "A new class of multifunctional reconfigurable antenna with continous beam steering capability," in *2022 IEEE International Symposium on Antennas and Propagation and USNC-URSI Radio Science Meeting (AP-S/URSI)*, 2022, pp. 808–809.

[14] S. S. Tathare and P. Goswami, "Design and development of a reconfigurable antenna with varactor diodes for next-generation wireless communication systems," *Computers and Electrical Engineering*, vol. 123, p. 110091, 2025. [Online]. Available: https://www.sciencedirect.com/science/article/pii/S0045790625000345

[15] R. E. Munson, "Microstrip phased array antennas," in *Proceedings of Twenty-Second Symposium on USAF Antenna Research and Development Program*, 1972.

[16] J. Howell, "Microstrip antennas," in *1972 Antennas and Propagation Society International Symposium*, vol. 10, 1972, pp. 177–180.

[17] R. Munson, "Conformal microstrip antennas and microstrip phased arrays," *IEEE Transactions on Antennas and Propagation*, vol. 22, no. 1, pp. 74–78, 1974.

[18] D. R. Jackson, *Antenna Engineering Handbook*. McGraw Hill, 2007, ch. 7 Microstrip Antennas, pp. 7–1–7–29.

[19] Bevelacqua. (2021) Microstrip antennas: The patch antenna. [Online]. Available: https://www.antenna-theory.com/antennas/patches/antenna.php

[20] L. Shafai, *Antenna Engineering Handbook*. McGraw Hill, 2007, ch. 16 Wideband Microstrip Antennas, pp. 16–1–16–47.

[21] D. Rodrigo, B. A. Cetiner, and L. Jofre, "Frequency, radiation pattern and polarization reconfigurable antenna using a parasitic pixel layer," *IEEE Transactions on Antennas and Propagation*, vol. 62, no. 6, pp. 3422–3427, 2014.

[22] A. Towfiq and B. A. Cetiner, "Reconfigurable antenna array of individual reconfigurable antennas," U.S. Patent 11,769,944 B2, Sep. 26, 2023.

[23] M. Zhang, G. Xu, and R. Gao, "Reconfigurable antennas for wireless communication: Design mechanism, state of the art, challenges, and future perspectives," *International Journal of Antennas and Propagation*, vol. 2024, no. 1, p. 3046393, 2024. [Online]. Available: https://onlinelibrary.wiley.com/doi/abs/10.1155/2024/3046393

[24] K. G. Darryn, "Low power reconfigurable antenna with continuous beam steering capability," Master's thesis, Utah State University, Logan, UT, 2021.

[25] D. Rodrigo, B. A. Cetiner, and L. Jofre, "Frequency, radiation pattern and polarization reconfigurable antenna using a parasitic pixel layer," *IEEE Transactions on Antennas and Propagation*, vol. 62, no. 6, pp. 3422–3427, 2014.

[26] Q. Chen, J. Ala-Laurinaho, A. Khripkov, J. Ilvonen, R. M. Moreno, and V. Viikari, "Varactor-based frequency-reconfigurable dual-polarized mm-wave antenna array for mobile devices," *IEEE Transactions on Antennas and Propagation*, vol. 71, no. 8, pp. 6628–6638, 2023.

[27] D. Garlotta, "A literature review of poly(lactic acid)," *Journal of Polymers and the Environment*, vol. 9, no. 2, pp. 63–84, Apr 2001. [Online]. Available: https://doi.org/10.1023/A:1020200822435

[28] T. Picha and S. Papezova, "Dielectric properties of materials for 3d printing at high frequencies," *Research in Agricultural Engineering*, vol. 69, no. 1, pp. 28–35, 2023.

[29] E. Huber, M. Mirzaee, J. Bjorgaard, M. Hoyack, S. Noghanian, and I. Chang, "Dielectric property measurement of pla," in *2016 IEEE International Conference on Electro Information Technology (EIT)*, 2016, pp. 0788–0792.

[30] S. Mufti, A. Tennant, and L. Seed, "3d electrically small dome antenna," in *2014 Loughborough Antennas and Propagation Conference (LAPC)*, 2014, pp. 653–656.

[31] E. Gupta, C. Bonner, N. Lazarus, M. S. Mirotznik, and K. J. Nicholson, "Multiaxis manufacture of conformal metasurface antennas," *IEEE Antennas and Wireless Propagation Letters*, vol. 22, no. 11, pp. 2629–2633, 2023.

[32] T. G. Spence, A. L. Ford, and C. C. Roberts, "Prototyping an s-band conformal line array antenna on a partial wing surface," in *2020 IEEE International Symposium on Antennas and Propagation and North American Radio Science Meeting*, 2020, pp. 1409–1410.

[33] Statasys. (2025) Ultem™ 9085 resin fdm® thermoplastic filament material data sheet. [Online]. Available: https://www.stratasys.com/contentassets/264560ca109a4876a3761fde68c3ab5e/mds_fdm_ultem9085_0525a.pdf?v=49972f

[34] R. P. H. Adji, D. P. Kurniadi, Taufiqqurrachman, A. B. Santiko, R. D. Mandasari, E. J. Pristianto, F. Darwis, A. N. Rahman, P. D. P. Adi, D. Kurnia, R. Pratindy, and A. A. Fathnan, "Low-cost 9.4 ghz microstrip patch antenna design with pla and copper tape," in *2024 International Conference on Radar, Antenna, Microwave, Electronics, and Telecommunications (ICRAMET)*, 2024, pp. 94–99.

[35] S. Masihi, M. Panahi, A. K. Bose, D. Maddipatla, A. J. Hanson, B. B. Narakathu, B. J. Bazuin, and M. Z. Atashbar, "Rapid prototyping of a tunable and compact microstrip antenna by laser machining flexible copper tape," in *2019 IEEE International Conference on Flexible and Printable Sensors and Systems (FLEPS)*, 2019, pp. 1–3.

[36] Ansys, Incorporated. (2025) Ansys hfss. [Online]. Available: https://www.ansys.com/products/electronics/ansys-hfss

[37] ——. (2013) An introduction to hfss: Fundamental principles, concepts, and use. [Online]. Available: https://athena.ecs.csus.edu/~milica/EEE212/HAND/HFSSintro.pdf

[38] I. MACOM. (2025) Ma4agfcp910. [Online]. Available: https://www.macom.com/products/product-detail/MA4AGFCP910

[39] I. Skyworks Solutions. (2025) Data sheet smv2019 to smv2023 series: Hyperabrupt junction tuning varactors. [Online]. Available: https://www.skyworksinc.com/-/media/864477E32CFA44658487FD52D57C7462.pdf

APPENDIX

Equation to Map Rectilinear Pixel Dimensions onto a Spherical Surface

In consequence of the spherical nature of the dome, the actual length of the pixels is longer than the planar length. The equation to find the actual length and width of the pixels is derived as follows:

Given two points located on a sphere of radius ρ centered at the origin, and the corresponding xy-coordinates given as $p_1 = (x_1, y_1)$ and $p_2 = (x_2, y_1)$, find the distance s between the points. Note that the points have the same y-coordinate.

The points may be considered to lie on a circle of radius r, which is the circle formed by the intersection of a plane given as (x, y_1, z) and the sphere of radius ρ. Note that the length ρ lies along the $\hat{x}$. The radius of the circle r is given by

$$r = \sqrt{\rho^2 - y_1^2} \tag{A.1}$$

The arc length between any two points on a circle is given by the equation

$$s = r\theta \tag{A.2}$$

where

s is the arc length between the two points

r is the radius of the circle

θ is the angle (in radians) between the two points

The angle between the z-axis and p_1 is $\theta_1 = sin^{-1}(\frac{x_1}{r})$. Likewise, the angle between the z-axis and p_2 is $\theta_2 = sin^{-1}(\frac{x_2}{r})$. Using Eqn. A.2 and subtracting one arc length from the other, we get

$$s = r\{sin^{-1}(\frac{x_1}{r}) - sin^{-1}(\frac{x_2}{r})\} \tag{A.3}$$

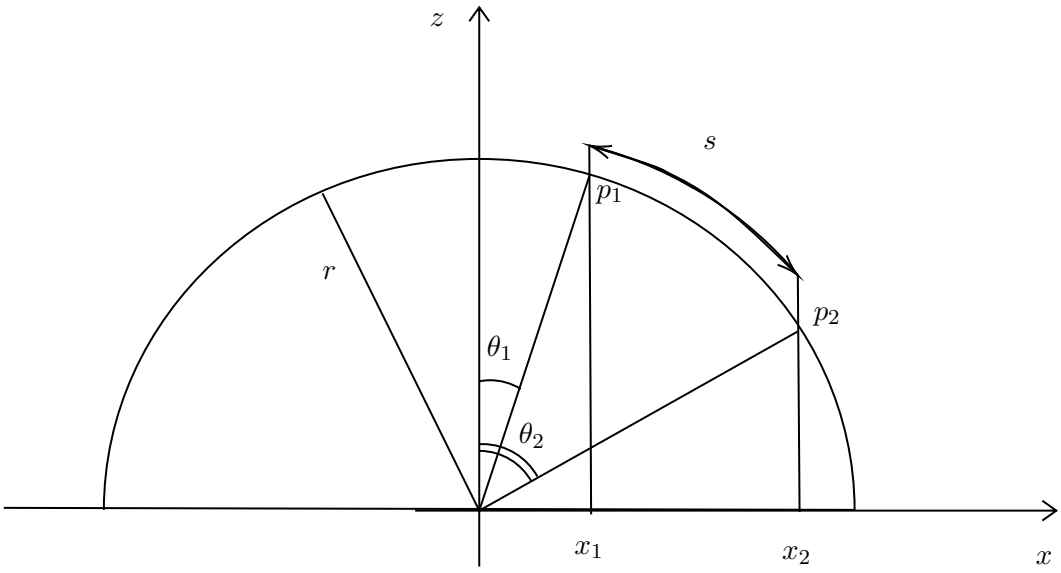

Fig. A.1: Diagram to illustrate Eqn. A.3. The semicircle shown is the intersection of a sphere of radius ρ and the plane along $y = y_1$ as described in the text.

It is worth noting that the dome is radially symmetric about $\hat{z}$. Therefore, the arc length between a pair of points with the same x-value and differing y-values may be found via appropriate substitutions.